SAND2007-0473J

A System Model for Assessing Scalar Dissipation Measurement Accuracy in Turbulent Flows

G-H. Wang[1], N.T. Clemens[2], R.S. Barlow[1]*, and P.L. Varghese[2]

1) Combustion research Facility

Sandia National Laboratories, Livermore, CA, 94551

2) Department of Aerospace Engineering and Engineering Mechanics

The University of Texas at Austin, Austin, TX, 78712

*Corresponding author: Robert S. Barlow

barlow@ca.sandia.gov

Combustion Research Facility

Sandia National Laboratories

Livermore, CA, 94550

A System Model for Assessing Scalar Dissipation Measurement Accuracy in Turbulent Flows

G-H. Wang[1], N.T. Clemens[2], R.S. Barlow[1*], and P.L. Varghese[2]

1) Combustion research Facility

Sandia National Laboratories, Livermore, CA, 94551

2) Department of Aerospace Engineering and Engineering Mechanics

The University of Texas at Austin, Austin, TX, 78712

Abstract: A system model is developed to investigate independent and coupled effects of resolution, noise, and data processing algorithms on the accuracy of the scalar gradient and dissipation measurements in turbulent flows. Finite resolution effects are simulated by spectral filtering, noise is modeled as an additive source in the model spectrum, and differencing stencils are analyzed as digital filters. In the current study, the effective resolution is proposed to be a proper criterion for quantifying the resolution requirement for scalar gradient and dissipation measurement. Both effective resolution and noise-induced apparent dissipation are mainly determined by the system transfer function. The finite resolution results, based upon a model scalar energy spectrum, are shown to agree with non-reacting experimental data. The coupled resolution-noise results show three regions in the mean scalar dissipation rate measurement: noise-dominant region, noise-resolution correlated region, and resolution-dominant region. Different noise levels lead to different resolution error curves for the measured mean scalar dissipation rate. Experimental procedures and guidelines to improve the scalar gradient and dissipation

experiments are proposed, based on these model study results. The proposed system approach can also be applied to other derived quantities involving complex transfer functions.

Keywords: Scalar dissipation; Turbulent flow; Measurement accuracy; Resolution; Noise

Nomenclature

a , b , c	coefficients in the high-order spectral-like stencil
B	box filter
C_{SR}	constant in the model spectrum of Smith-Reynolds
C_{CP}	constant in the model spectrum of Corssin-Pao
C_P, C_η , C_L	constants in the model spectrum of Pope
C_e	$C_e = \kappa_e / \kappa_{1C}$
D	scalar diffusivity [$m^2 s^{-1}$]
$D_1(\kappa_1)$, $D(\kappa)$	1D and 3D scalar dissipation spectrum
$E(\kappa)$	3D kinetic energy spectrum
$F_1(\kappa_1)$, $F(\kappa)$	1D and 3D scalar energy spectrum
$F_n(\kappa_1)$	1D noise floor
f_B	Batchelor frequency, $f_B = \langle U \rangle / 2\pi\lambda_B$ [s^{-1}]
f_L, f_η	non-dimensional functions in the model spectrum of Pope
g	gradient
G_N	noise gain factor for the numerical stencil
h_e	effective system filter, $h_e = h_g * h_p * h_r$
h_g	numerical stencil for gradient calculation
h_p	post-processing filter, e.g. smoothing
h_r	filter to simulate resolution effect
H_e	effective system transfer function, $H_e = H_g H_p H_r$
H_g, H_p, H_r	Fourier transforms of h_p, h_g and h_r, respectively
G, N	Fourier transforms of g and n
k	turbulent kinetic energy
L	turbulent outer length scale
L_θ	turbulent outer length scale for scalar
m	parameter in the model spectrum of Smith-Reynolds
n	noise
x	general coordinate component [m]
x_1, x_2, x_3	Cartesian coordinates [m]

Greek symbols

α , β	coefficients in the high-order spectral-like stencil
α_{SR}	parameter in the model spectrum of Smith-Reynolds
β_P	parameter in the model spectrum of Pope

χ	3D scalar dissipation rate [s^{-1}]
χ_1	1D scalar dissipation rate [s^{-1}]
χ_a	apparent scalar dissipation rate [s^{-1}]
Δ	sampling resolution [m]
$\Delta_e, \Delta_p, \Delta_r$	characteristic length scales of filters h_e, h_p and h_r, respectively [m]
ε	turbulent kinetic energy dissipation rate
$\in_\xi$	measurement error for quantity ξ
γ	resolving efficiency for the numerical stencil
γ_χ	resolving dissipation efficiency for the numerical stencil
Γ	Gamma function
η	Kolmogorov length scale, [m]
κ	wavenumber [rad m^{-1}]
κ_1	wavenumber along x_1 direction [rad m^{-1}]
κ_{1C}	cutoff wavenumber along x_1 direction, $\kappa_{1C} = \pi/\Delta = \kappa_{1S}/2$ [rad m^{-1}]
κ_{1S}	sampling wavenumber along x_1 direction [m^{-1}]
κ_B	Batchelor wavenumber [rad/m^{-1}], $\kappa_B = 1/\lambda_B$
κ_g	characteristic wavenumber of numerical stencil g [rad m^{-1}]
$\kappa_e, \kappa_r, \kappa_p$	characteristic wavenumber of filter h_e, h_r and h_p, respectively [rad m^{-1}] $\kappa_e = \pi/\Delta_e$, $\kappa_r = \pi/\Delta_r$ and $\kappa_p = \pi/\Delta_p$
κ_I	wavenumber corresponds to the integral length scale l [rad m^{-1}]
λ_B	Batchelor scale [m]
ν	kinematic viscosity of fluid [$m^2 s^{-1}$]
θ	scalar (e.g. mixture fraction, temperature)
θ_d	scalar after data-reduction
θ_m	measured scalar
θ_p	scalar after post-processing
Θ	Fourier transform of scalar θ
σ_{LSF}	standard deviation of LSF [m]
σ_n^2	variance of noise
ω	non-dimensional wavenumber, $\omega = \pi\kappa_1/\kappa_{1C}$
ξ	general quantity of interest, e.g. $\langle\theta^2\rangle$, $\langle\chi_1\rangle$

Dimensionless numbers

Re	Reynolds number
Re_L	outer-scale Reynolds number, $Re_L = \langle k\rangle^2 / \langle\varepsilon\rangle\nu$
Re_λ	Taylor microscale Reynolds number

Sc	Schmidt number, $Sc = \nu / D$

Mathematical operators

$\langle \cdot \rangle$	mean quantity
*	convolution operator
∇	gradient operator

Abbreviations

DNS	direct-numerical-simulation
FWHM	full width half maximum
H12B	1st-order 2-point one-side backward difference
H23C	2nd-order 3-point central difference
H67C	6th-order 7-point central difference
HA7I	10th-order 7-point high-order spectral-like implicit scheme
H47I	4th-order 7-point high-order spectral-like implicit scheme
H47J	4th-order 7-point high-order spectral-like implicit scheme (optimized)
LES	large eddy simulation
LSF	line spread function
MTF	modulation transfer function
NF	noise floor
PIV	particle image velocimetry
PSF	point spread function
rms	root mean square
SGS	sub-grid scale
SNR	signal-to-noise ratio
SS	sharp-spectral filter

Superscripts and subscripts

$'$	fluctuation quantity
*	normalized quantity
m	measured quantities
$i, (i)$	coordinate components in the x_i-direction, $i = 1$, 2 and 3

1 Introduction

The scalar dissipation rate — defined as $\chi = 2D|\nabla\theta|^2$, where θ is a conserved scalar and D is the molecular diffusivity — is important in scalar mixing because it is a measure of the rate at which inhomogeneities in the scalar property are removed by diffusion [1]. Furthermore, χ is particularly important in combustion because it is fundamentally related to the structure of turbulent nonpremixed flames and appears directly or indirectly in most turbulent combustion models [2-4]. Owing to its importance in turbulent mixing, a great deal of work has been directed at its measurement in turbulent flows and flames by applications of single- or two-point time-series measurement [5-13], 1D time-series measurements [14], 1D line imaging [15, 16], 2D planar and 3D imaging [17-22]. The accurate measurement of the scalar dissipation rate is very challenging, especially in turbulent reacting flows, due to the limited spatial resolution and low signal levels. Experimental and analytical results have shown that resolution and noise have opposite effects, since limited resolution acts to reduce scalar gradients [23, 24], whereas noise tends to increase the measured dissipation [25]. These coupled but opposing effects make the assessment of the experimental accuracy in dissipation measurements extremely difficult, which is illustrated in the recent study of spatial resolution and noise effects in scalar imaging experiments using Monte Carlo simulations [26].

Wyngaard [23] studied the effect of the hot-wire length on the spectra and variances of the stream-wise velocity and temperature fluctuations and gradients by using the model energy spectrum of Corrsin [27] and Pao [28]. The results suggest that the measured values of both velocity and scalar gradients decrease significantly as the probe length increases. Wyngaard [24] further found that the 1D spectrum is attenuated significantly when the wire length is sufficiently

long. Antonia and Mi [29] conducted spectral corrections for all the measured spatial derivatives of velocity and temperature fluctuations by using the isotropic relations to infer the 3D energy spectrum from the measured 1D spectrum of temperature. Their results showed that the measured derivative variances are highly sensitive to the separation between sensors. A model was developed to enable the prediction of resolution-induced errors in scalar gradients for individual dissipation structures [30]. The optical resolution effects on the measured dissipation layer thickness, peak gradient, and peak dissipation rate were determined for the case where the dissipation layer profile and the optical line spread function (LSF) can be approximated as Gaussian. It was concluded that, for a single dissipation layer structure, the layer thickness should be 7.5 times larger than the standard deviation of the LSF in order for the peak dissipation rate measurement error to be less than 10%.

Several studies have investigated the important effects of noise on scalar dissipation measurements. Noise effects are particularly important for laser scattering measurements, especially those that use Rayleigh or Raman scattering, since they tend to suffer from relatively low signal-to-noise ratio (SNR). Mi and Antonia [25] showed that the measured squared-gradient term for a passive scalar θ is $\left\langle (\partial\theta/\partial x)^2 \right\rangle_m = \left\langle (\partial\theta/\partial x)^2 \right\rangle + \left\langle n_1^2 + n_2^2 \right\rangle / \Delta^2$. Here $\langle\ \rangle$ indicates a time- or ensemble-averaging process, subscript m denotes the measured quantity, n_1 and n_2 are the noise levels at two adjacent points, and Δ is the separation between the two points. The noise-induced dissipation rate in practical measurements has been termed the "apparent dissipation" [31] and is given by $\left\langle n_1^2 + n_2^2 \right\rangle / \Delta^2$. The apparent dissipation is always positive, and so the measured squared-gradient is always higher than its true mean value. In fact, the apparent dissipation will tend to dominate at arbitrarily high resolution since $\left\langle (\partial\theta/\partial x)^2 \right\rangle \to constant$ and

$\left\langle n_1^2 + n_2^2 \right\rangle / \Delta^2 \to \infty$ as $\Delta \to 0$. The effect of noise on the measured mean scalar dissipation is particularly important in relatively low SNR measurements, such as those that employ gas-phase Raman [15, 16] and Rayleigh scattering [32, 33] in reacting flows.

The major difference between measurements of a scalar quantity as opposed to its gradient/dissipation is that the effects of the data processing, such as the smoothing filter and numerical stencil, are significant in the latter case and must be considered. Numerical stencil effects have been thoroughly investigated in computational fluid dynamics [34-38], but their influence on the accuracy of quantities derived from measurements has received less attention. Depending on the implicit or explicit nature of the numerical stencil used, the differentiation accuracy is not only affected by the sampling resolution, but the specific scheme as well, e.g. the resolving efficiency [34]. Pruett [39] pointed out that the finest physical scale is determined by the underlying physics, but the numerical differentiation accuracy is mandated by the chosen numerical stencil. The numerical stencil effects have been recognized in gradient related experiments, e.g. vorticity measurements using the Particle Image Velocimetry (PIV) technique [40-42].

In this context it should be emphasized that the measurement of the scalar dissipation rate is a system problem in which experimental factors, like optical system resolution, experimental noise, post processing filter, and numerical stencils act together to determine the measured value. Specifying only the experimental probe resolution, such as determined by the effects of probe length [23, 24, 29, 43, 44] and optical system blur [30], is not adequate for quantifying the resolution error of gradient-based measurements. It is the *effective resolution*, characterized by the overall system transfer function, that determines the true resolution of the measurement. This system view also suggests that grid convergence studies, which are sometimes used to determine

the finest dissipation scale [21], may only reflect the resolution for specific numerical schemes, i.e., the numerical resolution. Such tests may or may not be able to determine the underlying physical scale, and the measured dissipation rate may or may not be claimed to be fully-resolved. Furthermore, the noise-induced apparent dissipation is more complicated than assumed in the analysis by Mi and Antonia [25], because the effect of the specific numerical differentiation stencil was not considered. The numerical stencil affects both the effective resolution and apparent dissipation, and its effect must be accounted for.

The objective of the current study is to develop a more thorough understanding of the independent and/or coupled effects of the factors that influence dissipation measurements. The system model developed here is more comprehensive than previous models [23, 24, 29, 43, 44] and can be used for either time-series or spatially-resolved imaging data. The physical scales that are to be measured are modeled by using a model turbulent energy spectrum. The resolution effect is simulated by filtering the model spectrum in the spectral domain, similar to Mi and Nathan [45], and the noise effect is modeled as the additive uncorrelated noise floor superimposed on the model energy spectrum [25]. Reynolds number effects on the resolution requirements are compared with experimental data from nonreacting jets [45]. The available numerical schemes are so numerous that the range of possible combinations is overwhelming [34]. Therefore, procedures to select or design the optimum numerical stencil under certain experimental circumstances are presented. Among the various experimental techniques that are available to measure or derive the scalar dissipation rate [46], the current system model is focused on the direct approach where the scalar quantity is measured at adjacent points and its gradient is then calculated numerically.

Though the numerical results are limited by use of the model spectrum, the system model is generic, and some of these results apply to general gradient and dissipation related experiments. This study will be particularly important for scalar dissipation rate measurements where the dissipation length scale is unknown (e.g. turbulent flows in complex geometry, turbulent reacting flows) and the signal level is low [15, 16, 47, 48].

2 System model

Figure 1 shows a diagram of the system model for the measurement of the scalar dissipation rate χ, starting from the scalar distribution θ. The model is developed for 1D experiments, but it can be readily extended to the 2D and 3D cases. The system model incorporates several sub-models that represent experimental and numerical processes involved in obtaining the scalar gradient and dissipation. In the current system model there are several key processes: (1) The measured scalar signal is processed by an analog filter before being digitally sampled by the analog-to-digital converter. The analog filtering includes effects of anti-aliasing filters, averaging owing to finite probe/pixel length [23, 24, 29, 43], and optical blurring [30]. (2) Post-processing filters may be applied, for example to smooth noisy data. (3) Some data reduction procedure may be used, such as converting a Rayleigh scattering signal to temperature or mixture fraction. Such a procedure will be specific to a given experiment. (4) The sampled data are numerically differentiated to obtain the squared gradient of the measured scalar. (5) The squared gradient is multiplied by the diffusivity.

For 1D linear operations, these sub-models can be characterized as

$$\text{Measurement: } \theta_m = h_r * \theta + n, \tag{1}$$

$$\text{Post-processing: } \theta_p = h_p * \theta_m, \tag{2}$$

$$\text{Data-reduction: } \theta_p \rightarrow \theta_d \,, \tag{3}$$

$$\text{Gradient: } g = h_g * \theta_d \,, \tag{4}$$

$$\text{Dissipation: } \chi = 2D \,|\, g \,|^2 \,, \tag{5}$$

where h_r is the filter to simulate the resolution effect, n the noise, $*$ the convolution operator, θ_m the measured scalar quantity, h_p the post-processing filter, θ_p the post-processed scalar, θ_d the scalar after data-reduction, h_g the filter used to represent the gradient calculation, and g the computed gradient.

The measurement sub-model (1) includes resolution and noise effects. The resolution effect is modeled as a convolution of the scalar distribution with the analog filter, h_r. The noise effect is modeled as uncorrelated additive source. For example, photon shot noise can be approximated as an additive random source whose variance is proportional to the signal intensity for high signal levels. The post-processing sub-model (2) considers the effect of the post-processing filters, e.g. averaging, smoothing, pixel-binning, etc. Since the data reduction sub-model (3) is measurement technique dependent and it is not included in the development of the system model. The gradient sub-model (4) evaluates the effect of the numerical differentiation stencils. The gradient filter depends on both the sampling resolution and the specific numerical stencil used. The dissipation sub-model (5) mainly considers the effect of diffusivity, which is primarily important in flows with variable properties such as reacting flows. The importance of this is easily overlooked, but Geyer [49] showed that errors in the diffusivity may have a significant impact on the calculated mixture fraction dissipation in reacting flows.

In the following analysis, it is assumed that: (*i*) the data reduction process (3) is ignored; (*ii*) the diffusivity is constant, and so the mean squared-gradient term is used as a proxy for the

dissipation; (*iii*) noise is uncorrelated with the scalar quantity. Under these assumptions, the measured gradient may be expressed as

$$g_m = h_g * h_p * \left(h_r * \theta + n\right). \tag{6}$$

It can be seen that the derived gradient is affected jointly by the resolution, noise, post-processing filter, and the numerical scheme. Therefore, the effective system transfer function may be defined as

$$h_e = h_g * h_p * h_r, \tag{7}$$

In most optical diagnostics measurements, the noise and resolution are coupled. For example, larger pixel size of an array detector will lead to better SNR under the same incident light level because of the larger number of photons collected per pixel. For resolution-dependent noise, the system model can be written as,

$$g_m = h_g * h_p * h_r * \left(\theta + n\right). \tag{8}$$

These two gradient models are shown schematically in Fig. 2. In the Fourier domain, the above system models can be expressed as,

$$G_m = H_g H_p \left(H_r \Theta + N\right), \text{ for resolution independent noise source,} \tag{9}$$

$$G_m = H_g H_p H_r \left(\Theta + N\right), \text{ for resolution dependent noise source.} \tag{10}$$

where G_m, H_g, H_p, H_r, Θ and N are Fourier transforms of g_m, h_g, h_p, h_r, θ and n, respectively. In the following sections, it will be shown how these independent and/or coupled processes affect the measured gradient and dissipation rate.

3 Model scalar spectrum

For isotropic turbulent flow, Corrsin [27] and Pao [28] developed a 3D scalar energy spectrum,

$$F(\kappa) = C_{CP}\langle\chi\rangle\langle\varepsilon\rangle^{-1/3}\kappa^{-5/3}\exp\left(-\frac{3}{2}C_{CP}D\langle\varepsilon\rangle^{-1/3}\kappa^{4/3}\right) \text{ for } \kappa > \kappa_I\,, \tag{11}$$

where $\kappa = \sqrt{\kappa_1^2 + \kappa_2^2 + \kappa_3^2}$ is the magnitude of the wavenumber vector, $C_{CP} = 1.7$ [29, 50], $\langle\chi\rangle$ is the mean scalar dissipation rate, $\langle\varepsilon\rangle$ is the mean kinetic energy dissipation rate, κ is the wavenumber (with units of radians/length), and κ_I is the wavenumber corresponding to the integral length scale. This form was widely used in the correction of the finite probe length effects by Wyngaard [24], Antonia and Mi [29], and Mi and Nathan [45], and spatial averaging effects in reacting flows by Mansour et al. [51]. For small Schmidt number flows ($Sc = \nu/D$), the smallest spatial length scale is the Obukhov-Corrsin scale $\eta Sc^{-3/4}$ [52]. For large Schmidt numbers, the smallest length scale is the Batchelor scale [53], defined as $\lambda_B = \eta\, Sc^{-1/2}$. Batchelor scale is commonly referred as the finest mixing scale in turbulent mixing even though its definition is valid only for large Schmidt numbers [52]. In the current study, it is not necessary to distinguish between the Batchelor and Obukhov-Corrsin scales because we limit our discussion to the case of near unity Schmidt numbers when both scales are the same as the Kolmogorov scale.

The normalized wavenumber is calculated as $\kappa^* = \kappa/\kappa_B$, where $\kappa_B = 1/\lambda_B$ is the "Batchelor wavenumber", and corresponds to the cutoff frequency of the dissipation range. For gas flows with $Sc \approx 1$, the normalized energy spectrum is

$$F^*(\kappa^*) = C_{CP}(\kappa^*)^{-5/3} \exp\left(-\frac{3}{2} C_{CP}(\kappa^*)^{4/3}\right). \quad (12)$$

A modified version of this equation was developed by Smith and Reynolds [50] for the kinetic energy spectrum. However, it can be assumed that the normalized scalar energy spectrum is of the same form as the normalized kinetic energy spectrum for flows with $Sc \approx 1$. The Smith-Reynolds model spectrum is

$$F^*(\kappa^*) = C_{SR}(\kappa^*)^{-5/3} \exp\left\{-\alpha_{SR}(\kappa^*)^m\right\} \text{ for } \kappa > \kappa_I, \quad (13)$$

where $C_{SR} = 2$, $\alpha_{SR} = \left\{C_{SR}\frac{2}{m}\Gamma\left(\frac{4}{3m}\right)\right\}^{3m/4}$, Γ is the Gamma function, m is an appropriately chosen constant, and it is found that $m = 2$ matches experimental data better. The Corrsin-Pao spectrum is just a special case of the Smith-Reynolds model with $m = 4/3$ and $C_{SR} = 1.7$.

Both the Corrsin [27]-Pao [28] and Smith-Reynolds [50] model scalar energy spectra have an exponential decay in the high wavenumber region, a slope of -5/3 in the intermediate to low wavenumber range, and are accurate only in the high wavenumber range $\kappa > \kappa_I$. It is well known that for isotropic turbulence, the 3D spectrum approaches zero at low wavenumber, which is not reflected in either the Corrsin-Pao or Smith-Reynolds models. Therefore, these models are of limited value for studying quantities, such as the scalar variance, which are strongly affected by low wavenumber fluctuations. Using these energy spectrum models to analyze the measurement error in scalar variance due to finite resolution effects is questionable (e.g. Ref. [51]).

A correct model must consider the low wavenumber region to include relatively large scale turbulent motions. Pope [38] developed such a the model for the kinetic energy spectrum,

$$E(\kappa) = C_P \langle \varepsilon \rangle^{2/3} \kappa^{-5/3} f_L(\kappa L) f_\eta(\kappa \eta), \tag{14}$$

where f_L and f_η are non-dimensional functions defined as

$$f_L(\kappa L) = \left\{ \frac{\kappa L}{\sqrt{(\kappa L)^2 + C_L}} \right\}^{5/3 + p_0}, \tag{15}$$

$$f_\eta(\kappa \eta) = \exp\left\{ -\beta_P \left\{ \left[(\kappa \eta)^4 + C_\eta^4 \right]^{1/4} - C_\eta \right\} \right\}, \tag{16}$$

where $L = \langle k \rangle^{3/2} / \langle \varepsilon \rangle$ is a characteristic large-scale length scale, $\langle k \rangle$ is the mean kinetic energy, and $\eta = \left(\nu^3 / \langle \varepsilon \rangle \right)^{1/4}$ is the Kolmogorov scale. Pope [38] suggests the following values for the constants in Eqs. (14)-(16): $p_0 = 2$, $\beta_P = 5.2$, $C_P = 1.5$. C_η and C_L are determined by the requirement that the integrals of the energy and dissipation spectra over all wavenumbers are the mean kinetic energy and dissipation rate, respectively. At very high Reynolds number, the asymptotic values are $C_\eta = 0.40$ and $C_L = 6.78$. This model spectrum has p_0 scaling for low wavenumber, the classical $-5/3$ Kolmogorov scaling in the inertial range, and exponential decay in the dissipation range. With the knowledge of the model energy spectrum, the corresponding homogeneous dissipation spectrum is given by $2\nu\kappa^2 E(\kappa)$. An outer-scale Reynolds number can be defined based on the turbulence kinetic energy and dissipation as $\mathrm{Re}_L = \langle k \rangle^2 / \langle \varepsilon \rangle \nu$, which related to the Taylor scale Reynolds number by $\mathrm{Re}_\lambda = \sqrt{\frac{20}{3} \mathrm{Re}_L}$ as in [38]. For high Reynolds number turbulent flow, the relation between the large-scale length scale and the Kolmogorov scale is $\eta / L = \mathrm{Re}_L^{-3/4}$. Following the same argument as in the

Smith-Reynolds model spectrum for flows with $Sc \approx 1$, the normalized scalar energy spectrum is assumed to have the same form as the normalized kinetic energy spectrum [54],

$$F^*(\kappa^*) = C_P (\kappa^*)^{-5/3} f_L(\kappa^* \frac{L_\theta}{\lambda_B}) f_\eta(\kappa^*), \tag{17}$$

where $L_\theta \approx L$. The model energy spectrum is mainly a function of the normalized wavenumber κ^* and the length scale ratio L_θ / λ_B, which can be expressed in terms of the Reynolds number as $L_\theta / \lambda_B \approx L/\eta = \mathrm{Re}_L^{3/4}$ for $Sc \approx 1$.

For the case of large Schmidt number, the spectrum exhibits a viscous-convective subrange with a κ^{-1} scaling [52], and so the model spectra of Corrsin [27]-Pao [28], Smith-Reynolds [50] and Pope [38] are not appropriate. Model scalar energy spectra including Schmidt number effects have been proposed by Kraichnan [55], McComb [56] and Fox [57]. However, these models are relevant to high Sc number flows and so are not necessarily appropriate for gas phase studies. Nevertheless, the major objective of the current study is to introduce the system model approach, and so an appropriate model, such as Fox's, could be used to study the experimental effects of noise, resolution, data processing algorithms and numerical stencils on dissipation measurements in high Schmidt number flows.

With the definition of the 3D energy spectrum, the corresponding 1D scalar energy spectrum can be calculated as [38, 52, 58]

$$F_1(\kappa_1) = \int\int_{-\infty}^{\infty} \frac{F(\kappa)}{4\pi\kappa^2} d\kappa_2 \, d\kappa_3 . \tag{18}$$

The scalar dissipation spectrum and its normalized form are

$$D(\kappa) = 2D\kappa^2 F(\kappa), \tag{19}$$

$$D^*(\kappa^*) = 2(\kappa^*)^2 F^*(\kappa^*). \tag{20}$$

Figure 3 shows a comparison of the 3D model energy and dissipation spectra of Corrsin-Pao [27, 28], Smith-Reynolds [50] and Pope [38]. It can be seen clearly that both Corrsin-Pao and Smith-Reynolds 3D model spectra only capture the high wavenumber region ($\kappa > \kappa_I$) of the energy spectrum. Pope's model includes Reynolds number effects and matches experimental data in the literature [38]. Also, as expected, the dissipation spectra from all three models agree much better than the energy spectra, especially for the model from Smith-Reynolds [50] and Pope [38].

4 Results and discussion

The proposed system model will be used to study the independent and coupled effects of finite resolution, noise and numerical stencil, on the measured scalar gradient and dissipation rate. The analytic results and discussions are mainly for 1D data, but the system model can be easily extended to the 2D and 3D cases.

4.1 Resolution effect

The isolated effect of resolution is investigated by assuming that noise is negligible, and the differentiation is exact without numerical artifacts. For a measurement with finite resolution, the measured 1D scalar energy and dissipation spectra are related to corresponding true spectra as,

$$[F_1(\kappa_1)]_m = |H_r(\kappa_1, \kappa_r)|^2 F_1(\kappa_1), \tag{21}$$

$$[D_1(\kappa_1)]_m = |H_r(\kappa_1, \kappa_r)|^2 D_1(\kappa_1), \tag{22}$$

where $H_r(\kappa_1,\kappa_r)$ is the filter that represents the finite resolution effect and κ_r is the characteristic cutoff wavenumber of the filter. In the literature, various filter models have been used in the literature to approximate finite resolution as summarized in Table 1. They are similar to the low-pass filters used in large eddy simulation (LES) [37, 38]. Resolution effects are related both to "averaging" over the finite probe volume and "sampling" at known spatial frequency by the detector(s). Averaging is a common problem in practical experiments, such as finite wire length, array-detector pixel size, pixel binning, etc. In previous studies by Wyngaard [23, 24, 43], Antonia and Mi [29], and Mi and Nathan [45], averaging was modeled as a box filter, which implies that the signal is uniformly distributed along the finite wire length. In imaging experiments the averaging is due to the blurring effect of the imaging system, which is quantified by the optical system point spread function (PSF) and modulation transfer function (MTF) [30, 59]. The resolution effect due to finite sampling can be modeled by the sharp spectral filter if a relatively sharp spectral cutoff anti-aliasing filter is used.

By using the 1D model spectrum as the "true" spectrum, we can determine the ratio of the measured to the true variance from 1D measurements,

$$\left\langle \left(\theta^2\right)_m \right\rangle \Big/ \left\langle \theta^2 \right\rangle = \int_0^\infty \left[F_1(\kappa_1)\right]_m \, d\kappa_1 \Big/ \int_0^\infty F_1(\kappa_1)\, d\kappa_1 , \tag{23}$$

and the ratio of the measured to the true 1D mean scalar dissipation is

$$\left\langle \left(\chi_1\right)_m \right\rangle \Big/ \left\langle \chi_1 \right\rangle = \int_0^\infty \left[D_1(\kappa_1)\right]_m d\kappa_1 \Big/ \int_0^\infty D_1(\kappa_1)\, d\kappa_1 . \tag{24}$$

It can be seen clearly that both ratios are functions of the filter h_r. These forms have been used [24, 29, 45] with h_r represented by a box filter.

Using Eqs. (23) and (24), the measurement error due to finite resolution can be expressed as,

$$\in_{\xi} = 1 - \xi_m / \xi \,, \tag{25}$$

where $\xi = \langle \theta^2 \rangle$ and $\xi = \langle \chi_1 \rangle$ for scalar variance and 1D mean dissipation rate, respectively.

To simulate the resolution effect, three filter forms were used: box, sharp-spectral (SS) and Gaussian. Figure 4 shows the transfer functions of these filters for a normalized cutoff wavenumber of $\kappa_r^* = 0.5$. It can be seen that both box and Gaussian filters still have finite gain of 0.4 at $\kappa_1^* = 0.5$ and approach zero near $\kappa_1^* = 1$. This is different from the ideal sharp spectral filter, which exhibits no leakage for wavenumbers higher than the designed cutoff $\kappa_1^* = 0.5$. Figure 5 shows the filtered dissipation spectra using the same three low-pass filters with cut-off wavenumber of $\kappa_r^* = 0.5$. The leakage of the spectral energy beyond the cut-off wavenumber is expected considering Fig. 4. Figures 4 and 5 show that the box and Gaussian filters have nearly the same spectral behavior.

Figure 6 compares the averaging and sampling effects of different analog filters on the turbulent scalar variance and mean 1D scalar dissipation rate. To obtain the results in Fig. 6, it was assumed that the sampling resolution is high enough that there is no aliasing problem for averaging effects. Figure 6 shows that the finite resolution effects are nearly the same for the box and Gaussian filter, but are different for the sharp-spectral filter. At high resolution (large κ_r^*), the averaging error in the scalar dissipation is much larger for the box and Gaussian filters than for the sharp-spectral filter. Figure 6 essentially demonstrates that the effect of spatial averaging is much larger than that of finite sampling rate. Though the scalar variance is not very

sensitive to the finite resolution effect, Fig. 6a shows that the specific filter type does affect the error curve. This may be important when comparing experimental data with LES resolved fields and validating sub-grid-scale (SGS) modeling because the effective experimental filter may affect the results.

The measured data can be corrected for averaging effects due to filters shown in Fig. 6. For example, the finite wire length effect may be corrected before calculating the energy and dissipation spectrum in hot/cold wire experiments [29, 45]. Knowing the filter transfer function, the true energy spectrum can be corrected via

$$F_1(\kappa_1) = \left[F_1(\kappa_1)\right]_m \Big/ \left| H_r(\kappa_1,\kappa_r)\right|^2, \tag{26}$$

Several studies have been aimed at optimizing this deconvolution. The main difficulties are associated with the accurate measurement of the transfer function h_r and the presence of noise [60]. Various algorithms have been developed that reflect different ways to recover a *best* estimate of the *true* value. Wiener and regularized filters are better for the case where both the transfer function and noise characteristics are known [61, 62]. Some iterative restoration techniques [63], e.g. expectation maximization algorithms, work better for the case of a known transfer function but unknown noise characteristics. It should also be noted that in the presence of noise the transfer function of $1\Big/\left| H_r(\kappa_1,\kappa_r)\right|^2$ behaves like a high-pass filter which amplifies noise. Some of these issues will be discussed further in section 4.5.

Figure 7 compares the resolution effects simulated using different model spectra. These curves are referred as error curves for the variance and mean dissipation rate since they are directed related to the measurement error defined in Eq. (25). In the figure, f_r and f_B are the filter cut-off frequency and Batchelor frequency, respectively, and therefore $\kappa_r^* = f_r^*$, where

$f_r^* = f_r / f_B$. The Batchelor frequency is defined as $f_B = \langle U \rangle / 2\pi\lambda_B$, where $\langle U \rangle$ is the mean convection velocity [45]. Four different Reynolds numbers, $\mathrm{Re}_\lambda = 50$, 130, 500 and 1500, are used for Pope's model spectrum. As shown in Fig. 7, the ratio of $\langle (\theta^2)_m \rangle / \langle \theta^2 \rangle$ and $\langle (\chi_1)_m \rangle / \langle \chi_1 \rangle$, decrease roughly linearly for the former and exponentially for the latter case with decreasing resolution (increasing $1/\kappa_r^*$). As discussed in section 3 (Fig. 3a), the Corrsin-Pao and Smith-Reynolds model spectra do not consider the low wavenumber effects, and thus studying resolution effects on the measured variance using these two model spectra will not give the correct trend, which is clearly shown in Fig. 7a. Pope's model spectrum with $\mathrm{Re}_\lambda = 130$ can match the jet flow experimental data ($\mathrm{Re}_\lambda = 180$) in Mi and Nathan [45]. Using Pope's model with different Reynolds numbers as in Fig. 7a, it is seen that the resolution effect on the scalar variance is Reynolds number dependent, i.e. smaller error at higher Reynolds number. However, the resolution effect on mean scalar dissipation rate is not so sensitive to the Reynolds number, as seen in Fig. 7b. This is expected since the variance is mainly affected by the large scales whose characteristics are more sensitive to Reynolds number. Figure 7b also shows that results from different models can give nearly the same resolution error curve for the 1D mean dissipation rate.

Note that the large scales can depend strongly on the flow geometry, so the model spectrum used here is not expected to be universally applicable with regard to large turbulent scales and the associated effect of resolution on the variance. This is not a limitation of the present work, because the system model presented here may be applied to any model spectrum or to experimental data.

4.2 Noise effect

If noise is uncorrelated with the signal, it may be modeled as an additive source to the measured spectrum. In this case the measured scalar is $\theta_m = \theta + n$, and the measured scalar energy and dissipation spectra can be expressed as,

$$\left[F_1(\kappa_1)\right]_m = F_1(\kappa_1) + F_n(\kappa_1), \tag{27}$$

$$\left[D_1(\kappa_1)\right]_m = 2D\,\kappa_1^2\left[F_1(\kappa_1) + F_n(\kappa_1)\right]. \tag{28}$$

For white noise, the noise spectrum is flat in the spectral domain (noise floor), as illustrated in Fig. 8a. The noise spectrum is modeled as

$$F_n(\kappa_1) = \sigma_n^2 / \kappa_{1C}\,, \tag{29}$$

where $\kappa_{1C} = \pi/\Delta$ and Δ is the sampling resolution. Equation (29) satisfies the relation $\sigma_n^2 = \int_0^{\kappa_{1C}} F_n(\kappa_1)\,d\kappa_1$, and so the noise-induced apparent dissipation may be calculated as

$$\chi_a = \frac{2}{3} D \sigma_n^2 \kappa_{1C}^2\,. \tag{30}$$

From these relations, the SNR for turbulence variance can be defined to quantify the noise induced error for the scalar variance measurement as

$$SNR_V = \left\langle \theta^2 \right\rangle / \sigma_n^2\,. \tag{31}$$

Similarly, the SNR for the dissipation rate can be expressed as

$$SNR_\chi = \frac{\langle \chi_1 \rangle}{\chi_a} = \frac{3}{2D}\langle \chi_1 \rangle \frac{1}{\sigma_n^2 \kappa_{1C}^2}. \tag{32}$$

The definitions of SNR_V and SNR_χ are illustrated in Fig. 8.

The SNR_V and SNR_χ are similar to the conventional SNR, $SNR = \langle \theta \rangle / \sigma_n$, in that all of them are inversely proportional to the standard deviation of the noise. However, the SNR_χ is highly resolution dependent as it also depends on the sampling wavenumber, i.e., $SNR_\chi \propto 1/\kappa_{1C}^2$. It can be seen clearly in Fig. 8 that the apparent dissipation increases without bound with increasing resolution. Once the cut-off wavenumber κ_{1C} is higher than the dissipation cut-off wavenumber (i.e., $\kappa_{1C}^* > 1$), then the mean value of the true dissipation rate $\langle \chi_1 \rangle$ will remain constant with further increase in the wavenumber. Therefore, the unnecessary high resolution will significantly amplify the noise induced apparent dissipation rate and reduce the SNR_χ, as illustrated by Fig. 8.

To further illustrate the noise effect on the scalar energy and dissipation spectra, Pope's model spectrum with $\mathrm{Re}_\lambda = 130$ is used to generate Fig. 9. We note that the model energy and dissipation spectra shown in the figure exhibit strong resemblance to experimentally measured spectra that exhibit significant noise effects [10, 64]. For SNR_V = 5, 20, 50, 100 and 500, the corresponding SNR_χ = 0.05, 0.22, 0.55, 1.1 and 5.81, respectively. To calculate the SNR_χ in Fig. 9, the sampling frequency is taken as twice the cut-off wavenumber, i.e., $\kappa_{1C}^* = 1$. SNR_V = 100 implies that the noise induced variance is only about 1% of the true scalar variance. However, the corresponding SNR_χ = 1.1 suggests that the noise induced dissipation is 91% of the true scalar dissipation, or equivalently, the apparent dissipation is about 48% of the measured

total dissipation rate. Figure 9 clearly illustrates this effect, small noise effects in the scalar variance can lead to significant measurement error in the mean 1D scalar dissipation rate.

4.3 Combined resolution and noise effect

In most laser diagnostics experiments, changing resolution will affect the noise characteristics, for example, by changing CCD pixel size, laser beam thickness or pixel binning. Here the energy and dissipation spectra may be modeled as

$$\left[F_1(\kappa_1)\right]_m = \left|H_r(\kappa_1,\kappa_r)\right|^2\left[F_1(\kappa_1)+F_n(\kappa_1)\right], \tag{33}$$

$$\left[\chi_1(\kappa_1)\right]_m = 2D\kappa_1^2\left|H_r(\kappa_1,\kappa_r)\right|^2\left[F_1(\kappa_1)+F_n(\kappa_1)\right]. \tag{34}$$

It can be seen from section 4.1 and 4.2 that insufficient resolution will result in a measured scalar dissipation rate below the true value. Conversely, noise induced apparent dissipation always adds to the measured dissipation rate. The combined effect of resolution and noise makes the assessment of the experimental accuracy in dissipation measurements particularly challenging. Figure 10 shows the measurement error in the scalar variance and mean dissipation rate as a function of resolution for different levels of noise using Eq. (33) and (34), which assume that the noise is resolution dependent. The noise effect is smaller for the scalar variance than for the scalar dissipation because the variance is dominated by large-scale high-magnitude fluctuations, which are relatively insensitive to all but the lowest SNR_V. In contrast, the dissipation is much more sensitive to the noise and the noise effect increases greatly at high bandwidth as shown in Eq. (30). Figure 10b shows that if there is noise present in the signal, the measured dissipation greatly overshoots the true dissipation as resolution improves (large κ_r^*). It is seen that the noisier the data, the more improved resolution comes at the cost of increased

error. All noise error curves collapse at low resolution because the averaging effects at low bandwidth effectively increase the SNR of the measurements as seen in Eq. (33) and (34).

These same effects are shown schematically in Fig. 11. For noise-free scalar dissipation measurements, the resolution error is represented by the solid line in Fig. 11, which is similar to the curve in Fig. 2 of Mi and Nathan [45]. For the noise-free case there is no measurement error when the spatial resolution is smaller than or equal to $\kappa_1^* = 1$. However, in the presence of noise, the ratio of the measured to the true scalar dissipation grows without bound as the spatial resolution becomes higher, which agrees with the analysis of Mi and Antonia [25]. This is the noise-dominant regime, denoted as I in Fig. 11, where the measured scalar dissipation is always higher than the true scalar dissipation and the error generally increases with increasing noise level. In the noise and resolution dominant regime, denoted as II in Fig. 11, the effects of finite resolution and noise compete with each other to determine the measurement error. Interestingly, the measurement error is smaller than the noise-free (i.e., resolution only) error curve as shown in Fig. 11. This illustrates that at moderate resolution and moderate noise level, the measurement of mean scalar dissipation can be brought closer to the true mean value by the presence of noise. This seemingly counter-intuitive result is because noise-induced apparent dissipation offsets the attenuated dissipation resulting from finite resolution. However, it is not a useful strategy to improve the accuracy of a dissipation measurement by working in this regime because it is hard to know the noise level and resolution in actual experiments, and so the accuracy would be difficult to determine. At low resolution (large $1/\kappa_r^*$), the averaging effect is so dominant that the noise is not important at all. This is the resolution-dominant regime. In this case, the error curve collapses to the noise-free error curve and the measured mean dissipation rate is much

smaller than the true value. Figure 11 clearly illustrates the intricate relation between resolution and noise in scalar dissipation measurements.

4.4 Gradient Stencil Effect

The theoretical relationship between the scalar energy and dissipation spectra given by Eq. (19) assumes ideal differentiation in the spectral domain. For data analysis in the spatial or time domains, numerical stencils must be used to approximate the derivative. Furthermore, numerical differentiation is usually applied after the experimental data are measured, therefore it will affect both the resolution and noise-induced apparent dissipation for the calculated dissipation rate. For simplicity we first ignore the effects of the stencil on the noise, in which case the dissipation spectrum can be approximated as

$$\left[D_1(\kappa_1)\right]_m = 2D\left|H_g(\kappa_1,\kappa_{1C})\right|^2\left[F_1(\kappa_1)\right]_m, \tag{35}$$

where $\kappa_{1C} = \pi/\Delta = \kappa_{1S}/2$ is the cutoff wavenumber, κ_{1S} the sampling wavenumber, and Δ is the sampling resolution.

First order two-point backward difference stencils (H12B) and second-order central difference stencils (H23C), are commonly used to calculate the gradient. High-order spectral-like stencils have also been developed to evaluate the scalar derivatives in computational fluid dynamics [34, 65], which may be expressed as

$$\beta g_{i-2} + \alpha g_{i-1} + g_i + \alpha g_{i+1} + \beta g_{i+2} = c\frac{\theta_{i+3} - \theta_{i-3}}{6\Delta} + b\frac{\theta_{i+2} - \theta_{i-2}}{4\Delta} + a\frac{\theta_{i+1} - \theta_{i-1}}{2\Delta}, \tag{36}$$

where parameters α, β, a, b, and c are determined by substituting Taylor series expansion coefficients, and g represents the implicitly determined local derivative of the scalar. The

parameters α, β, a, b, and c are different for different order of accuracy and number of stencil points used. Table 2 lists coefficients for several high-order schemes, for example H67C denotes 6th-order 7-point central difference, HA7I the10th-order 7-point implicit scheme, H47I 4th-order 7-point implicit scheme and H47J the optimized 4th-order 7-point implicit scheme.

The system transfer function of the high-order stencil is

$$H_g(\kappa_1,\kappa_{1C}) = j\frac{\kappa_{1C}}{\pi}\frac{a\sin(\omega)+b\sin(2\omega)/2+c\sin(3\omega)/3}{1+2\alpha\cos(\omega)+2\beta\cos(2\omega)}, \tag{37}$$

where $\omega = \pi\kappa_1/\kappa_{1C}$ and $j=\sqrt{-1}$. The ideal 1D stencil is $H_g(\kappa_1,\kappa_{1C}) = j\kappa_1$. The capability of a particular numerical stencil to match the ideal stencil can be quantified by its resolving efficiency γ [34],

$$\gamma = \kappa_g/\kappa_{1C}, \tag{38}$$

where κ_g is the wavenumber at which the error between the filter magnitude transfer function and the ideal stencil is less than a certain tolerance, for example $1-\left|H_g(\kappa_1,\kappa_{1C})/\kappa_1\right| = 1\%$. The numerical schemes discussed by Lele [34] have relatively higher resolving efficiency than the H23C and H12B. Table 3 lists several numerical stencils for gradient calculation, and their characteristics are compared in Fig 12. It can be clearly seen that all these numerical stencils are essentially digital filters and mainly differ at the high wavenumber end. For example, the ideal and H12B stencils are high pass filters, and the high-order spectral-like filters are band-pass filters, which can match the ideal stencil in the low wavenumber region and attenuate the spectrum at the high wavenumber end. The H23C central differencing is band-pass as well, but its attenuation is significantly larger than the high-order spectral-like stencils. Following the

same optimizing procedure as in Lele [34] and Kim and Lee [65], a set of new coefficients (H47J) was found with resolving efficiency of 0.90 which is higher than those from the filter coefficients of Lele [34] (γ =0.84) and Kim and Lee [65] (γ =0.89).

If we assume that the physical cut-off wavenumber is the Batchelor wavenumber, and we want wavenumbers below this cut-off to be free of stencil affects, then we require $\kappa_g \geq \kappa_B$, or equivalently,

$$\kappa_{1C} \geq \kappa_B / \gamma \ . \tag{39}$$

Using this criterion, the implicit sharp-spectral like high order stencils H47I and HA7I in Table 3 have a less demanding for the required sampling resolution to resolve the Batchelor wavenumber.

The stencil effect should be considered especially when the sampling resolution is smaller than or close to the physical limiting length scale. This is because the characteristic transfer function of the numerical stencil (h_g) is directly linked to the cutoff wavenumber κ_{1C}. Figure 13 shows stencil effects on the dissipation spectra for two cases of digital sampling: "fully resolved" and "over-resolved". In the fully resolved case the filter cut-off is at the physical limiting scale, i.e. $\kappa_{1C}^* = 1$, and the sampling wavenumber is $\kappa_{1S}^* = 2$ (Nyquist sampling). The over-resolved case is over-sampled by a factor of two, i.e., $\kappa_{1C}^* = 2$ and $\kappa_{1S}^* = 4$. Figure 13 shows that both the H12B and H23C stencils significantly attenuate the true dissipation spectrum for the "fully resolved" case. The central difference stencil (H23C) does particularly poorly, and the figure shows that the use of such a stencil can significantly degrade the mean dissipation even though the measurements may be nominally fully resolved. Figure 13 further shows that the dissipation spectrum is reproduced better for both H12B and H23C when over-resolved by a

factor of two, but the central difference stencil still exhibits non-negligible error. Also shown in Fig. 13 is the H47I scheme, which reproduces the dissipation spectrum very accurately at both resolutions. It can be concluded that if the data are sampled at Nyquist rate $\kappa_{1S}^{*}=2$, the 4th-order scheme can be used to faithfully reproduce the dissipation scales.

To quantify the capability of a numerical stencil to resolve the mean 1D dissipation rate, the *dissipation resolving efficiency* γ_χ may be defined as

$$\gamma_\chi = \langle (\chi_1)_m \rangle (\kappa_{1C}^{*}) / \langle \chi_1 \rangle , \tag{40}$$

where $\langle (\chi_1)_m \rangle (\kappa_{1C}) = \int_0^{\kappa_{1C}} 2D \left| H_g(\kappa_1, \kappa_{1C}) \right|^2 F_1(\kappa_1) d\kappa_1$. Smaller values of γ_χ correspond to poorer resolving capability.

It should be noted that the resolving efficiency γ is different from the dissipation resolving efficiency γ_χ, since the former is determined by the ratio of wavenumbers as in Eq. (38), whereas the latter is based on the mean dissipation rate. The resolving efficiency γ may be more appropriate for numerical simulations, since the numerical stencil will not only affect the resolved mean dissipation, but the accumulation and propagation of numerical errors as well [37]. Therefore, it should be expected that for the same turbulent flow, numerical simulations using finite difference stencils should have relatively more stringent resolution requirements than corresponding experiments. Table 3 and Fig. 14 also compare the resolving capabilities of several numerical stencils in the literature. It can be seen that at $\kappa_{1C}^{*}=1$, there will be a 27% and 9% error in the measured mean dissipation rate for the H23C and H12B stencils, respectively. To fully resolve the total mean dissipation rate (e.g. γ_χ=99%), the sampling wavenumbers are 13.1 and 6.5 for H23C and H12B stencils. Therefore, the central differencing

scheme H23C is not suggested for the scalar gradient and dissipation calculation when the sampling resolution is smaller than or close to the required physical resolution. On the other hand, higher-order spectral-like stencils proposed by Lele [34], have much higher resolving capabilities. For example, for a sampling frequency of $\kappa_{1S}^{*}=2$, stencils HA7I, H47I and H47J resolve at least 98% of the total dissipation rate. Hence, when the sampling frequency is low, the high-order spectral-like schemes are much better than H23C and H12B.

From a resolution point of view, the central difference stencil (H23C) is the worst performer even compared to the one-sided difference stencil (H12B). However, considering the effects of noise, the H12B stencil acts as a high-pass filter that amplifies noise in the measured mean dissipation rate. In the presence of noise, the capability of the numerical stencil to amplify/attenuate the apparent dissipation may be expressed as,

$$G_N=\int_0^{\kappa_{1C}}\left|H_g\left(\kappa_1,\kappa_{1C}\right)\right|^2\,d\kappa_1\Big/\int_0^{\kappa_{1C}}\kappa_1^2\,d\kappa_1\,, \tag{41}$$

which is the ratio of the noise induced apparent dissipation from numerical stencil to that of the ideal stencil. It should be noted that the gain factor G_N is independent of the sampling wavenumber and is purely determined by the stencil type. Gain factors for different stencils are shown in Fig. 15. All stencils have smaller gain factor than the ideal stencil (Eq. 19), which suggests that the noise induced apparent dissipation is smaller than that from the ideal stencil.

Considering both resolution and noise effects, the high-order spectral-like stencils [34] reduce the apparent dissipation due to their band-pass nature, and they largely match the ideal stencil because of their high resolving efficiency. Therefore, this type of stencil is recommended for processing of experimental data in scalar gradient and dissipation measurements.

4.5 Noise reducing techniques

Experimental data are generally contaminated by noise, and some kind of post-processing filter h_p is often applied to remove noise. For example, Mi and Nathan[31] used a low pass filter to eliminate the effect of noise above the Batchelor frequency. Miller and Dimotakis[11] used a one-pole low-pass filter, Dowling[10] and Dowling and Dimotakis[9] used optimal and Gaussian filters, respectively. However, filtering essentially forces the high wavenumber end of the dissipation spectrum to resemble the transfer function of the filter. This is not necessarily a problem, provided the characteristics of the dissipation spectrum are known as in nonreacting isotropic turbulent flows. For general flow conditions a proper post processing filter may be designed if the dissipation spectrum is measured without significant noise effects and the experiment is fully-resolved. The function of this filter is to suppress noise without attenuating the true dissipation. The design criteria are to keep the filtered measured scalar $h_p * \theta_m$ close to its true value θ, while reducing noise as much as possible. If noise is uncorrelated with the signal, the filter transfer function may be expressed as,

$$\left|H_p\left(\kappa_1,\kappa_p\right)\right|^2 = \frac{\left[F_1\left(\kappa_1\right)\right]_m - F_n\left(\kappa_1\right)}{\left[F_1\left(\kappa_1\right)\right]_m}, \tag{42}$$

where κ_p is the characteristic wavenumber of the post-processing filter h_p. This implies that a filter in physical space may be designed to remove the noise effect when the noise floor can be determined. Eq. (42) is a special type of the Wiener filter [62] and general digital filters may also be designed to match this transfer function [61].

Some nonlinear filters, such as anisotropic [66] and median filters [61], have been applied in signal and image processing. However, most of these filters are limited to the scalar

itself and their effects on the measured scalar dissipation rate and scalar gradient are usually quantified by "grid convergence" type characterization. Some other noise correction techniques have also been summarized by Wang et al. [67]

4.6 Effective resolution

It is important to emphasize that the effective resolution of any gradient and dissipation measurement depends on both the physical (optical) resolution and the processing schemes that are applied. For example, if a very poor optical system is used, the whole system can be dominated by this limiting optical resolution rather than the often reported pixel resolution. Furthermore, the numerical schemes for calculating the gradient should be considered not only in terms of the order of accuracy (such as the truncation error), but also in terms of their impact on the resolution, especially in the presence of noise. The system-view also highlights the important distinction between the dissipation scale and the resolution required to resolve it. The dissipation scale is determined purely by the underlying physics, while the resolution requirements are affected by every process in the measurement/analysis system.

To consider coupled effects of these factors, the measured scalar energy and dissipation spectrum may be expressed as

$$\left[F_1(\kappa_1)\right]_m = \left|H_p(\kappa_1,\kappa_p)\right|^2 \left|H_r(\kappa_1,\kappa_r)\right|^2 F_1(\kappa_1), \tag{43}$$

$$\left[\chi_1(\kappa_1)\right]_m = 2D\left|H_g(\kappa_1,\kappa_{1C})\right|^2 \left|H_p(\kappa_1,\kappa_p)\right|^2 \left|H_r(\kappa_1,\kappa_r)\right|^2 F_1(\kappa_1). \tag{44}$$

The effective system transfer function may be expressed as $H_e = H_g H_p H_r$. A characteristic filter cut-off wavenumber κ_e may be defined based on the transfer function H_e, which is analogous to κ_r for the filter H_r. The measured 1D dissipation spectrum may be written as,

$$\left[\chi_1(\kappa_1)\right]_m = 2D\left|H_e(\kappa_1,\kappa_e)\right|^2 F_1(\kappa_1). \tag{45}$$

The cut-off wavenumber of a filter may be expressed in terms of the sampling wavenumber, such as $\kappa_e = C_e\kappa_{1C}$, where C_e is a constant. Therefore, the effective resolution requirement to resolve the physical spatial content up to κ_B is $\kappa_e \geq \kappa_B$, which may also be written as

$$\Delta \leq C_e\pi/\kappa_B\ , \tag{46}$$

This shows that the spatial resolution required to resolve the Batchelor wavenumber κ_B is not unique in practical experiments or numerical simulations, and must be determined from an overall system view as discussed here.

One subtle question is how to determine the characteristic cutoff length scale or wavenumber of a filter. Pope [38] defines the cutoff of the box and Gaussian filters as the wavenumber κ_r where the magnitudes of the transfer functions have the same value, e.g. $\left|H_r(\kappa_1,\kappa_r)\right| = 0.64$ as shown in Fig. 4. However, for some time-series experiments, the 3 dB cutoff is adopted, giving $\left|H_r(\kappa_1,\kappa_r)\right| = 1/\sqrt{2} \approx 0.71$. These examples show that even with the same filter, different definitions of the characteristic cutoff length scale will result in different measurement error curves as in Fig. 6 and 7. Furthermore, if we consider two different experiments where the shapes of the system transfer functions are different, then the two measurements may have different measurement errors even though the cutoff frequencies for the two transfer functions are the same. To avoid the ambiguity caused by different definitions of cutoff frequency, it is probably best to base the resolution requirement on the frequency required to resolve some fraction of a mean physical quantity (say 99% of the mean kinetic energy). A similar resolution requirement was previously proposed for LES [68]. Still, even this method is

not ideal because the resolution requirement will depend on the physical quantity of interest (e.g., whether the variance or mean dissipation is used). Though such a measure is not unique, it only depends on the quantity of interest and is not subject to the definition of the characteristic cutoff length scale.

The dissipation wavenumber κ_B determined from the dissipation spectrum is an ensemble of the scalar dissipation rate conditioned on the wavenumber or spatial length scale. Nonreacting experiments and theory show that the dissipation is highly intermittent [1, 69] and the dissipation structure thicknesses are generally distributed over a range of length scales [17-20]. There will be some intense but sparse behavior with significantly higher dissipation rate than average value [69]. The quantification of the resolution based on the mean dissipation value is therefore only statistically meaningful and can only give the correct mean dissipation rate. This criterion may not be adequate for measurements of instantaneous dissipation structures and higher order moments of the scalar dissipation. Therefore, it is questionable whether it is a sufficient criterion to measure the PDF of the scalar dissipation or the PDF of the dissipation structure thickness.

4.7 Example 1: spatial averaging along other directions

The effect of spatial averaging along the non-gradient direction has been widely recognized in hot/cold-wire experiments in nonreacting flows, but not as much in laser diagnostics experiments, especially for reacting flows. For example, consider a laser scattering measurement where the laser beam is relatively large in diameter, but where the averaging effects along the laser beam (due to optical blurring and pixel averaging) are very small. In other words the resolution is excellent in the direction of interest but compromised in the two orthogonal directions. The question to be addressed here is how the measured gradient in the x_1 direction is

affected by spatial averaging in the x_2 and x_3 directions. This has been studied by Wyngaard [23], who investigated spatial resolution requirements when measuring vorticity with hot-wire arrays. He used a box filter to model the spatial averaging effect of the hot-wires. Here we will show this effect in a more general approach.

The measured 1D energy spectrum, including resolution effects in directions other than the x_1 direction, is given by

$$\left[F_1(\kappa_1)\right]_m = \int\int_{-\infty}^{\infty} \left|H_r^{(i)}\left(\kappa_i, \kappa_r^{(i)}\right)\right|^2 \frac{F(\kappa)}{4\pi\kappa^2} d\kappa_2 d\kappa_3 \,, \tag{47}$$

where $i = 1$, 2 and 3 corresponds to the x_1, x_2 and x_3 directions, $H_r^{(i)}\left(\kappa_i, \kappa_r^{(i)}\right)$ and $\kappa_r^{(i)}$ are the filter transfer function and its characteristic cutoff wavenumber in the i^{th} direction, respectively. The case of $i = 1$ corresponds to the case where the resolution effect is in the x_1 direction only, i.e., where resolution is perfect in the x_2 and x_3 directions. This case was discussed previously in section 4.1. After substituting Eq. (47) into Eqs. (23) and (24), the ratio of the measured to the true values of the variance and 1D mean dissipation rate may then be determined.

If the averaging effects are in more than one direction, the measured 1D energy spectrum may be written as

$$\left[F_1(\kappa_1)\right]_m = \int\int_{-\infty}^{\infty} \left|H_r\left(\kappa_1, \kappa_2, \kappa_3, \kappa_r^{(1)}, \kappa_r^{(2)}, \kappa_r^{(3)}\right)\right|^2 \frac{F(\kappa)}{4\pi\kappa^2} d\kappa_2 d\kappa_3 \,, \tag{48}$$

where $H_r\left(\kappa_1, \kappa_2, \kappa_3, \kappa_r^{(1)}, \kappa_r^{(2)}, \kappa_r^{(3)}\right)$ is the general form of the filter to simulate the finite resolution effects. If the resolution effects along different directions are independent, Eq. (48) can be simplified as

$$\left[F_1(\kappa_1)\right]_m = \int\int_{-\infty}^{\infty} \prod_{i=1}^{3} \left|H_r^{(i)}\left(\kappa_i, \kappa_r^{(i)}\right)\right|^2 \frac{F(\kappa)}{4\pi\kappa^2}\, d\kappa_2 d\kappa_3 \,. \tag{49}$$

Figure 16 shows the simulated resolution effects due to averaging in the x_2 and x_3 directions with $H_r^{(2)} = H_r^{(3)}$ and $\kappa_r^{(2)} = \kappa_r^{(3)}$, and perfect resolution in the x_1 direction. In the figure, $i = 2$ indicates averaging in one orthogonal direction only, $i = 2{+}3$ indicates averaging in two orthogonal directions. In the simulation, the case $i = 2{+}3$ assumes that the finite resolution effects can be separated as in Eq. (49).

Since the model spectrum assumes isotropic turbulence, the results for the $i = 2$ and $i = 3$ will be identical, and thus only $i = 2$ is shown in Fig. 16. It can be seen clearly in Fig. 16 that spatial averaging in one orthogonal (x_2 or x_3), or both orthogonal directions (x_2 and x_3) has smaller effect on the x_1-gradients than when the averaging occurs in the x_1 direction only. For example, for the box filter, at $1/\kappa_r^* = 2$, the errors due to finite resolution along x_1 (direction of interest), x_2, and $x_2 + x_3$, are 29%, 12% and 21%, respectively.

Figure 16 illustrates an important point for practical measurements. As discussed in section 4.2 and 4.5, the noise can be reduced by applying a post-processing filter h_p, which may lead to some averaging effect. An effective way to reduce the noise effect without greatly sacrificing the resolution is to filter the signal in the directions other than the direction of interest. In the simulation we assumed the gradients are distributed isotropically. For anisotropic flows, when the measured gradient is along the major gradient component direction, the resulting finite resolution error along non-gradient direction will be even smaller than those in Fig. 16. For example, the radial gradient tends to be much higher than those along the axial and azimuthal directions in turbulent jet flames at radial locations near the reaction zone. Therefore, in such

experiments, the resolution along the radial direction should be kept as high as possible, and resolution in the other two directions can be compromised. These are particularly useful for laser diagnostic techniques where it may be difficult to reduce the laser beam thickness to smaller than ~200 μm, such as when an extended focal spot (i.e., Rayleigh range) is desired [59]. For planar and 1D imaging laser diagnostic experiments, the effective approach is to achieve high resolution along the laser beam direction and align the laser beam with the direction of the highest gradient.

4.8 Example 2: effects due to pixel binning

As another example of the application of the system model, we will model the effect of pixel binning on 1D imaging measurements of the scalar dissipation. The results from this section have important implications for the resolution of measurements that utilize on-chip binning of CCD detectors as well as gated integration with time-series measurements [15, 16, 70, 71]. As stated previously, a 1D array detector both averages due to the finite pixel size and digitally samples at a frequency determined by the pixel spacing (pitch). Both these effects lead to measurement errors since averaging causes gradient smoothing and insufficient sampling frequency induces aliasing. As a way to distinguish these effects, consider two different 1D array detectors with the same sampling frequency (i.e., same pixel pitch Δ) but different pixel averaging (i.e., different pixel size Δ_r) as shown in Fig. 17. The situation shown schematically in Fig. 17 can be realized in practice by array-detectors with different fill factors. The fill factor is defined as the fraction of the pixel area that is photosensitive. In Fig. 17 the cases of 25% and 100% fill factor are shown. A detector that samples with minimal averaging effects will have a negligible fill factor, but of course will suffer from poor SNR ratios because it will collect very

few photons. Binning is the process of combining adjacent pixels into an array of superpixels, and thus it affects both the averaging and sampling frequency.

In 1D imaging, the averaging effects may be modeled as a box filter followed by digital sampling. This is different from the analysis in section 4.1, where we assumed that the sampling frequency was high enough that only spatial averaging effects needed to be considered. The box filter has the characteristic filter width of Δ_r (pixel size) and the sampling resolution is Δ (pixel pitch). There are two characteristic cutoff frequencies that describe the system, namely, κ_r and κ_{1C}. For imaging, the pixel width Δ_r can be no larger than the pixel pitch Δ, and so the cutoff of the anti-aliasing filter is equal to or higher than the cutoff frequency, i.e. $\Delta_r \le \Delta$ or $\kappa_r \ge \kappa_{1C}$. In Fig. 17, the small fill-factor array will have four times the value of κ_r and so have smaller averaging effects, but both arrays have equal κ_{1C}. There are three important cases to consider when an imaging system is used to resolve the dissipation scales: (*i*) fully resolved, which occurs for $\kappa_B \le \kappa_{1C} \le \kappa_r$, (*ii*) resolved / aliased, which occurs for $\kappa_{1C} \le \kappa_B \le \kappa_r$, and (*iii*) under-resolved / aliased, which occurs for $\kappa_{1C} \le \kappa_r \le \kappa_B$.

To illustrate the imaging system effects on the measured scalar dissipation rate, we assume that the lens blurring effects are negligible and the pixel fill factor is 100% ($\kappa_{1C} = \kappa_r$). Figure 18 shows the 1D scalar energy and dissipation spectra for four binning cases corresponding to cutoff wavenumbers of κ_{1C}^* = 0.2, 0.5, 1.0 and 2.0, respectively. As discussed in section 4.1, the box filter's transfer function still has finite response at the cutoff wavenumber κ_r. Therefore, when the cutoff wavenumber is less than the Batchelor wavenumber, i.e. $\kappa_{1C}^* < 1$, the measured 1D scalar energy spectrum will be aliased. The aliasing leads to a deviation from the ideal spectrum but is hard to see in Fig. 18a. The aliasing effects are more readily observed

in the dissipation spectrum as shown in Fig. 18b, because it is in this wavenumber range where the dissipation is largest. We see that the aliasing manifests itself as a local rise in the spectrum at wavenumbers just below the cutoff frequency.

Figure 19 compares the measurement error due to pixel binning with that of pure spatial averaging due to the sharp-spectral and box filters. Owing to aliasing effects, the measurement errors for the scalar variance and 1D dissipation rate are both smaller than the corresponding values of the box filter. This is expected since the aliasing will transfer some of the scalar energy and dissipation from high to low wavenumbers, as shown in Fig. 18. The aliasing resulting from the unresolved part of the scalar energy spectrum increases experimental uncertainty, and this uncertainty will be hard to quantify.

The above analysis can also be applied to time-series measurements that employ a gated-integrator for which an external anti-aliasing filter is not used [33, 72]. In this case the gated integrator averages all fluctuations over the gate width and serves as an implicit anti-aliasing filter whose cutoff wavenumber is determined by the gate width. The subsequent number of gates per second determines the system sampling frequency. In a gated-integrator based measurement, usually the gate width is usually much smaller than the sampling period, i.e. $\Delta_t << \Delta$, which leads to negligible averaging effects, but significant aliasing errors.

4.9 Summary

It should be emphasized that all experimental data are *filtered* to some extent. The characteristics of the effective filter and the quantity of interest determine the measurement quality. The results developed above are mainly discussed in terms of the spectral domain for cases where closed-form expressions for the experimental factors like resolution, noise and numerical stencil can be obtained. For complex systems where non-linear transfer functions may

be used, such as with the application of a noise-reducing median filter in post-processing, the system model may not be expressed in the spectral domain. Here, the spatial expressions as in Eqs. (6) and (8) can be used to study these effects by numerical simulations, e.g. Monte Carlo simulations by Ghandhi [26].

Though the system model is developed mainly for the scalar gradient and dissipation rate measurement, the model itself is more generic. For example, the system model can be combined with the kinetic energy spectrum model of Wyngaard [24] and Antonia and Mi [29] to study the effects of experimental factors on the measurement accuracy of the velocity gradient, vorticity, kinetic dissipation rate, etc. Furthermore, the proposed system model approach can also be applied to study other derived quantities, e.g. higher order derivatives. As discussed earlier, the numerical results are limited by use of the model spectrum. However, if high fidelity DNS data were available, it could be used to replace the model spectrum, and numerical results could be obtained following the present system approach.

The proposed system approach may also be useful for preparing experimental or DNS data for the purpose of validating LES results, and for developing LES sub-grid scale models [37, 73-75]. Both experimental data and LES results represent filtered flow fields, though the filters involved may have significant different characteristics. The system approach can provide more objective validation of the LES by revealing possible artifacts from the measurements as well as the simulations.

5 Conclusions

A system model was used to study independent and coupled effects of optical resolution, noise, data processing, and differentiation stencil on the accuracy of scalar gradient and dissipation measurements. Finite resolution effects were simulated by spectral filtering, noise was modeled

as an additive source in the model spectrum, and differencing stencils were analyzed as digital filters. The "effective resolution" is proposed as a useful means of quantifying the resolution reduction owing to these combined effects. Both effective resolution and noise-induced apparent dissipation are determined by the system transfer function. The results for the coupled effects of noise and resolution show three regions in the mean scalar dissipation rate measurement: noise-dominated region, noise-resolution correlated region, and resolution-dominated region. Different noise levels lead to different resolution error curves for the measured mean scalar dissipation rate. The resolution error curve for scalar dissipation is not significantly affected by Reynolds number (at least for isotropic turbulence), but the error curve for scalar variance is. The model also shows that spatial averaging in directions orthogonal to the measurement direction has a smaller effect on resolution than when the averaging occurs in the measurement direction. These results are an extension to the work by Wyngaard [23, 24, 43], Antonia and Mi [29], and Mi and Nathan [45], Wang and Clemens [30], and Mueschke and Andrews [44] that only considered the resolution effect; by Ghandhi [26] on numerical simulation of resolution and noise effects; and by Lourenco and Krothapalli [42], Etebari and Vlachos [40], and Foucaut and Stanislas [41] on numerical stencil effects. Experimental procedures and guidelines to improve the scalar gradient and dissipation experiments are proposed based on these model study results. The proposed system approach can be applied to other derived quantities involving complex transfer functions. It can also be useful for the preparation of experimental or DNS data used for LES validation, and in the development of LES sub-grid scale models.

Acknowledgement

This work was supported by the National Science Foundation under grant CTS-9977481 and the U. S. Department of Energy, Office of Basic Energy Sciences, Division of Chemical Sciences,

Geosciences, and Biosciences. Sandia National Laboratories is a multiprogram laboratory operated by Sandia Corporation, a Lockheed Martin Company, for the United States Department of Energy under contract DE-AC04-94-AL85000.

References

[1] Sreenivasan K R and Antonia R A 1997 Phenomenology of small-scale turbulence *Annu. Rev. Fluid Mech.* **29** 435-472.

[2] Bilger R W 1976 The structure of diffusion flames *Combust. Sci. Technol.* **13 (1-6)** 155-170.

[3] Peters N, *Turbulent Combustion*, Cambridge University Press, Cambridge, UK, 2000.

[4] Veynante D and Vervisch L 2002 Turbulent combustion modeling *Prog. Energy Combust. Sci.* **28 (3)** 193-266.

[5] Antonia R A, Satyaprakash B R and Hussain A K M F 1980 Measurements of dissipation rate and some other characteristics of turbulent plane and circular jets *Phys. Fluids* **23 (4)** 695-700.

[6] Antonia R A, Satyaprakash B R and Hussain A K M F 1982 Statistics of fine-sacle velocity in turbulent plane and circular jets *J. Fluid Mech.* **119** 55-89.

[7] Antonia R A and Mi J 1993 Temperature dissipation in a turbulent round jet *J. Fluid Mech.* **250** 531-551.

[8] Mi J, Antonia R A and Anselmet F 1995 Joint statistics between temperature and its dissipation rate components in a round jet *Phys. Fluids* **7 (7)** 1665-1673.

[9] Dowling D R and Dimotakis P E 1990 Similarity of the concentration field of gas-phase turbulent jets *J. Fluid Mech.* **218** 109-141.

[10] Dowling D R 1991 The estimated scalar dissipation rate in gas-phase turbulent jets *Phys. Fluids A* **3** 2229-2246.

[11] Miller P L and Dimotakis P E 1996 Measurements of Scalar Power Spectra in High Schmidt Number Turbulent Jets *J. Fluid Mech.* **308** 129-146.

[12] Tong C and Warhaft Z 1995 Passive scalar dispersion and mixing in a turbulent jet *J. Fluid Mech.* **292** 1-38.

[13] Wang D and Tong C 2002 Conditionally filtered scalar dissipation, scalar diffusion, and velocity in a turbulent jet *Phys. Fluids* **14** 2170-2185.

[14] Pitts W M, Richards C D and Levenson M S, Large- and small-scale structures and their interactions in an axisymmetric jet, NISTIR-6393, National Institute of Standards and Technology, 1999.

[15] Karpetis A N and Barlow R S 2002 Measurements of scalar dissipation in a turbulent piloted methane/air jet flame *Proc. Combust. Inst.* **29** 1929-1936.

[16] Barlow R S and Karpetis A N 2004 Measurements of scalar variance, scalar dissipation, and length scales in turbulent piloted methane/air jet flames *Flow, Turb. Combust.* **72 (2-4)** 427-448.

[17] Buch K A and Dahm W J A 1996 Experimental study of the fine-scale structure of conserved scalar mixing in turbulent shear flows. Part 1. Sc»1 *J. Fluid Mech.* **317** 21-71.

[18] Buch K A and Dahm W J A 1998 Experimental study of the fine-scale structure of conserved scalar mixing in turbulent shear flows, Part 2. Sc≈1 *J. Fluid Mech.* **364** 1-29.

[19] Su L K and Clemens N T 1999 Planar measurements of the full three-dimensional scalar dissipation rate in gas-phase turbulent flows *Exp. Fluids* **27** 507-521.

[20] Su L K and Clemens N T 2003 The structure of fine-scale scalar mixing in gas-phase planar turbulent jets *J. Fluid Mech.* **488** 1-29.

[21] Dahm W J A and Southerland K B, Quantitative flow visualization via fully-resolved four-dimensional imaging, in: Smits A J and Lim T T (Eds.), *Flow Visualization Techniques and Examples*, Imperial College Press, London, 2000, pp. 289-316.
[22] Tsurikov M S, Experimental Investigation of The Fine Scale Structure in Turbulent Gas-Phase Jet Flows, Ph.D. thesis, The University of Texas at Austin, 2002.
[23] Wyngaard J C 1969 Spatial resolution of the vorticity meter and other hot-wire arrays *J. Sci. Instrum.* **2** 983-987.
[24] Wyngaard J C 1971 Spatial resolution of a resistance wire temperature sensor *Phys. Fluids* **14 (9)** 2052-2054.
[25] Mi J and Antonia R A 1994 Some checks of Taylor's hypothesis in a slightly heated turbulent circular jet *Exp. Thermal Fluid Sci.* **8 (4)** 328-335.
[26] Ghandhi J B 2006 Spatial resolution and noise considerations in determining scalar dissipation rate from passive scalar image data *Exp. Fluids* **40 (4)** 577-588.
[27] Corrsin S 1964 Further generalization of Onsager's cascade model for turbulent spectra *Phys. Fluids* **7** 1156-1159.
[28] Pao Y H 1965 Structure of turbulent velocity and scalar fields in large wave-numbers *Phys. Fluids* **8** 1063-1075.
[29] Antonia R A and Mi J 1993 Corrections for velocity and temperature derivatives in turbulent flows *Exp. Fluids* **14 (3)** 203-208.
[30] Wang G-H and Clemens N T 2004 Effects of imaging system blur on measurements of flow scalars and scalar gradients *Exp. Fluids* **37 (2)** 194-205.
[31] Nandula S P, Brown T M and Pitz R W 1994 Measurements of scalar dissipation in the reaction zones of turbulent nonpremixed H_2-air flames *Combust. Flame* **99 (3-4)** 775-783.
[32] Ferrão P, Heitor M V and Salle R, On the accuracy of scalar dissipation measurements by laser Rayleigh scattering, 10th International Symposium on Turbulence, Heat and Mass Transfer, Lisbon, Portugal, 2000.
[33] Wang G-H, Clemens N T and Varghese P L 2005 High-repetition rate measurements of temperature and thermal dissipation in a non-premixed turbulent jet flame *Proc. Combust. Inst.* **30** 691-699.
[34] Lele S K 1992 Compact finite difference schemes with spectral like resolution *J. Comp. Phys.* **103 (1)** 16-42.
[35] Moin P and Mahesh K 1998 Direct numerical simulation: a tool in turbulence research *Annu. Rev. Fluid Mech.* **30** 539-578.
[36] Mahesh K 1998 A family of high order finite difference schemes with good spectral resolution *J. Comp. Phys.* **145** 332-358.
[37] Sagaut P, *Large Eddy Simulation for Incompressible Flows: An Introduction*, Third ed., Springer, New York, 2005.
[38] Pope S B, *Turbulent Flows*, Cambridge University Press, Cambridge, UK, 2000.
[39] Pruett C D, Toward the de-mystification of LES, in: *Toward the de-mystification of LES*, Liu C, Sakell L and Beutner T, (Eds.), Greyden Columbus, OH, 2001, pp. 231-238.
[40] Etebari A and Vlachos P P 2005 Improvements on the accuracy of derivative estimation from DPIV velocity measurements *Exp. Fluids* **39 (6)** 1432-1114.
[41] Foucaut J M and Stanislas M 2002 Some considerations on the accuracy and frequency response of some derivative filters applied to particle image velocimetry vector fields *Meas. Sci. Technol.* **13 (7)** 1058-1071.

[42] Lourenco L and Krothapalli A 1995 On the accuracy of velocity and vorticity measurements with PIV *Exp. Fluids* **18 (6)** 421-428.
[43] Wyngaard J C 1968 Measurement of small-scale turbulence structure with hot wires *J. Sci. Instrum.* **1** 1105-1108.
[44] Mueschke N J and Andrews M J 2005 Investigation of scalar measurement error in diffusion and mixing processes *Exp. Fluids* **40 (2)** 165-175.
[45] Mi J and Nathan G J 2003 The influence of probe resolution on the measurement of a passive scalar and its derivatives *Exp. Fluids* **34 (6)** 687-696.
[46] Stewart E J and Huq P 2006 Dissipation rate correction methods *Exp. Fluids* **40 (3)** 405-421.
[47] Barlow R S and Karpetis A N 2005 Scalar length scales and spatial averaging effects in turbulent piloted methane/air jet flames *Proc. Combust. Inst.* **30** 673-680.
[48] Karpetis A N and Barlow R S 2005 Measurements of flame orientation and scalar dissipation in turbulent partially premixed methane flames *Proc. Combust. Inst.* **30** 665-672.
[49] Geyer D, 1D-Raman/Rayleigh Experiments in A Turbulent Opposed-Jet, Ph.D. thesis, Technical University of Darmstadt, 2004.
[50] Smith L M and Reynolds W C 1991 The dissipation-range spectrum and the velocity-derivative skewness in turbulent flow *Phys. Fluids A* **3 (5)** 992-994.
[51] Mansour M S, Bilger R W and Dibble R W 1990 Spatial-averaging effects in Raman/Rayleigh measurements in a turbulent flame *Combust. Flame* **82 (3-4)** 411-425.
[52] Tennekes H and Lumley J L, *A First Course in Turbulence*, MIT Press, Cambridge, MA, 1972.
[53] Batchelor G K 1959 Small-scale variation of convected quantities like temperature in a turbulent fluid. Part 1. General discussion and the case of small conductivity *J. Fluid Mech.* **5** 113-133.
[54] Pantano C and Sarkar S 2001 A subgrid model for nonlinear functions of a scalar *Phys. Fluids* **13 (12)** 3803-3819.
[55] Kraichnan R H 1974 Convection of a pasive scalar by a quasi-uniform random straining field *J. Fluid Mech.* **64** 737-762.
[56] McComb W D, *The Physics of Fluid Turbulence*, Oxford University Press, Oxford, 1990.
[57] Fox R O, *Computational Models for Turbulent Reacting Flows*, Cambridge University Press, Cambridge, UK, 2003.
[58] Hinze J O, *Turbulece*, 2nd ed., McGraw-Hill, New York, 1975.
[59] Clemens N T, Flow Imaging, in: Joseph P H (Ed.) *Encyclopedia of Imaging Science and Technology*, John Wiley and Sons, New York, 2002, pp. 390-419.
[60] Lagendijk R L and Biemond J, Basic methods for image restoration and identification, in: Bovik A (Ed.) *Handbook of image and video processing*, Academic Press, San Diego, CA, 2000.
[61] Oppenheim A V, Schafer R W and Buck J R, *Discrete-time signal processing*, 2nd ed., Prentice Hall, Upper Saddle River, NJ, 1999.
[62] Vaseghi S V, *Advanced Digital Signal Processing and Noise Reduction*, Second ed., John Wiley & Sons, New York, 2000.
[63] Moon T K 1996 The Expectation-Maximization Algorithm *IEEE Signal Processing Magazine* **13 (6)** 47-60.

[64] Mi J, Deo R C and Nathan G J 2005 Fast-convergent iterative scheme for filtering velocity signals and finding Kolmogorov scales *Phys. Rev. E* **71** 066304.
[65] Kim J W and Lee D J 1996 Optimized compact finite difference schemes with maximum resolution *AIAA J.* **34 (5)** 887-893.
[66] Malm H, Hult J, Sparr G and Kaminski C F 2000 Non-linear diffusion filtering of images obtained by planar-laser-induced fluorescence spectroscopy *J. Opt. Soc. Am. A* **17 (12)** 2148-2156.
[67] Wang G-H, Clemens N T and Varghese P L 2005 Two-point, high-repetition-rate Rayleigh thermometry in flames: Techniques to correct for apparent dissipation induced by noise *Appl. Opt.* **44** 6741-6751.
[68] Pope S B 2004 Ten questions concerning the large-eddy simulation of turbulent flows *New J. Phys.* **6** 35.
[69] Sreenivasan K R 2004 Possible effects of small-scale intermittency in turbulent reacting flows *Flow, Turb. Combust.* **72 (2-4)** 115-131.
[70] Wang G-H, Barlow R S and Clemens N T 2006 Quantification of resolution and noise effects on thermal dissipation measurements in turbulent non-premixed jet flames *Proc. Combust. Inst.* **31** doi:10.1016/j.proci.2006.07.242.
[71] Wang G-H, Karpetis A N and Barlow R S 2006 Dissipation length scales in turbulent nonpremixed jet flames *Combust. Flame* doi:10.1016/j.combustflame.2006.09.005.
[72] Panda J and Seasholtz R G 2002 Experimental investigation of density fluctuations in high-speed jets and correlation with generated noise *J. Fluid Mech.* **450** 97-130.
[73] Oefelein J C, Schefer R W and Barlow R S 2006 Toward validation of large-eddy simulation for turbulent combustion *AIAA J.* **44 (3)** 418-433.
[74] Pitsch H 2006 Large-Eddy Simulation of turbulent combustion *Annu. Rev. Fluid Mech.* **38** 453-482.
[75] Veynante D and Knikker R 2006 Comparison between LES results and experimental data in reacting flows *J. Turb.* **7 (35)** 1-20.

Tables

Table 1. Examples of filter h_r and corresponding transfer function H_r for simulating finite resolution effect. B denotes the box function and relation between the characteristic cutoff wavenumber κ_r and the cutoff length scale Δ_r is $\kappa_r = \pi/\Delta_r$.

Name	Spatial domain $h(x,\Delta_r)$	Spectral domain $H(\kappa_1,\kappa_r)$	Reference
Box	$\frac{1}{\Delta_r} B\left(\frac{1}{2}\Delta_r - \lvert x\rvert\right)$	$\frac{\sin(\kappa_1\Delta_r/2)}{(\kappa_1\Delta_r/2)}$	Wyngarrd [23, 24, 43], Antonia and Mi [29], Mi and Nathan [45]
Gaussian	$\left(\frac{6}{\pi\Delta_r}\right)^{1/2} \exp\left(-\frac{6x^2}{\Delta_r^2}\right)$	$\exp\left(-\frac{\kappa_1^2\Delta_r^2}{24}\right)$	Wang and Clemens [30], Pope [38]
Sharp spectral	$\frac{\sin(\pi\ x/\Delta_r)}{\pi\ x}$	$B\left(\frac{\pi}{\Delta_r} - \lvert\kappa_1\rvert\right)$	Pope [38]

.

Table 2. High-order sharp spectral type numerical stencil coefficients [34].

Scheme	α	β	a	b	c
H23C	0	0	1	0	0
H67C	0	0	3/2	-3/5	1/10
HA7I	1/2	1/20	17/12	101/150	1/100
H47I	0.5771439	0.0896406	1.3025166	0.9935500	0.03750245
H47J	0.5828481	0.0911561	1.2923271	1.0217251	0.03395610

Table 3. Resolving properties of numerical stencils.

Scheme	γ [1]	γ_χ [2]	κ_{1S}^* [3]	Description
H23C	0.08	0.73	13.1	2nd-order 3-point central difference
H12B	0.16	0.91	6.5	1st-order 2-point one-side backward difference
H67C	0.35	0.92	3.5	6th-order 7-point central difference
HA7I	0.68	0.98	2.3	10th-order 7-point implicit scheme
H47I	0.84	0.99	2.1	4th-order 7-point implicit scheme
H47J	0.90	0.99	2.1	4th-order 7-point implicit scheme (optimized)

Note: 1. Resolving efficiency γ for $H_g(\kappa_1, \kappa_{1C})/\kappa_1 = 99\%$.

2. Resolving dissipation efficiency $\gamma_\chi = \langle (\chi_1)_m \rangle (\kappa_{1C}) / \langle \chi_1 \rangle$ at $\kappa_{1S}^* = 2$ (Nyquist sampling).

3. Sampling wavenumber κ_{1S}^* for $\gamma_\chi = 99\%$.

Figures

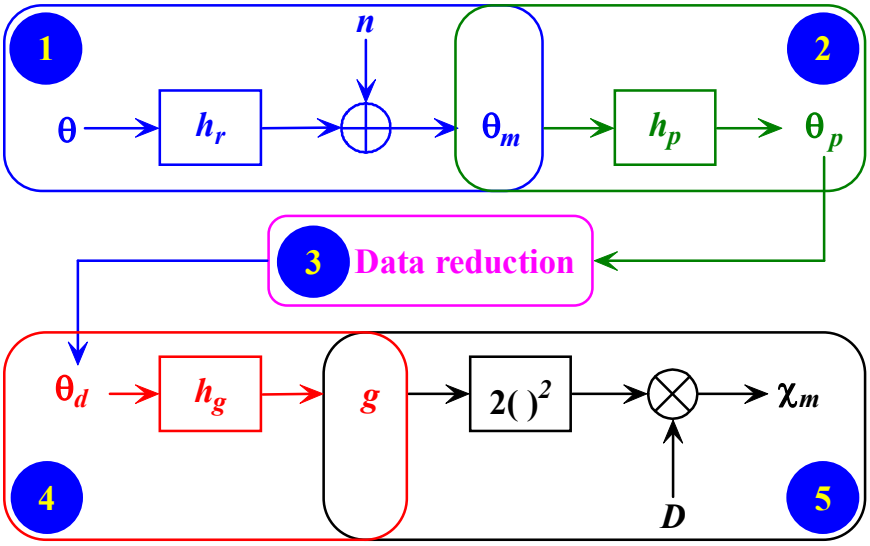

Figure 1. System model from scalar field θ to the scalar dissipation rate χ, where θ is the scalar, h_r is the low-pass filter to simulate resolution effect, n is the noise, θ_m is the measured scalar, h_p is the post-processing filter, θ_p is the post-processed data, θ_d is the data after data reduction, h_g is the digital filter for gradient calculation, g is the computed gradient, D is the diffusivity, and χ_m is the measured scalar dissipation rate.

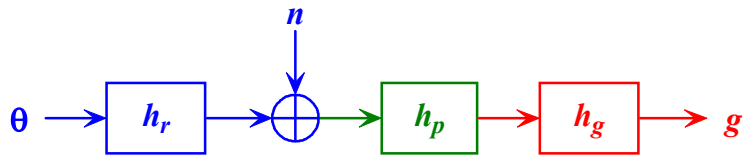

(a)

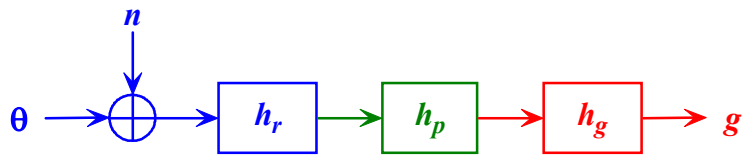

(b)

Figure 2 Simplified system model from scalar θ to gradient g: (a) noise is independent of resolution; (b) noise and resolution are correlated.

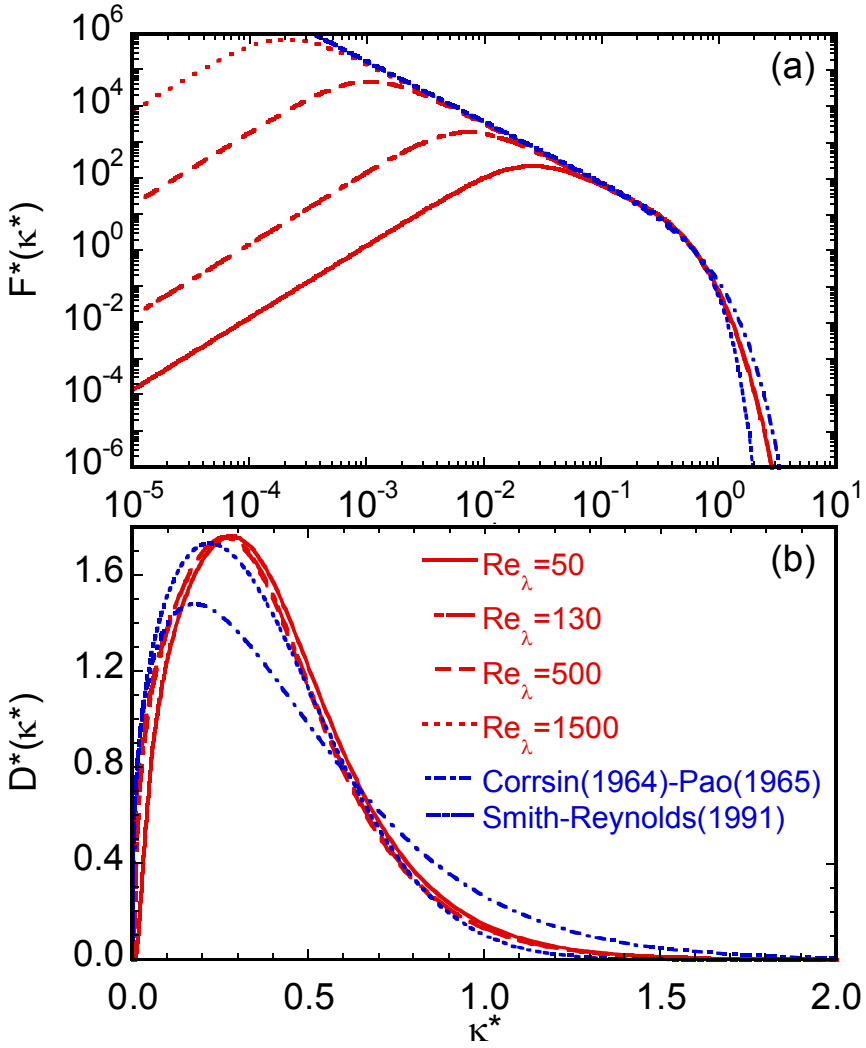

Figure 3 Comparing 3D model scalar energy and dissipation spectra by Pope [38], Corrsin [27]-Pao [28], and Smith-Reynolds [50]. (a) 3D scalar energy spectrum $F^*(\kappa^*)$; (b) 3D scalar dissipation spectrum $D^*(\kappa^*)$

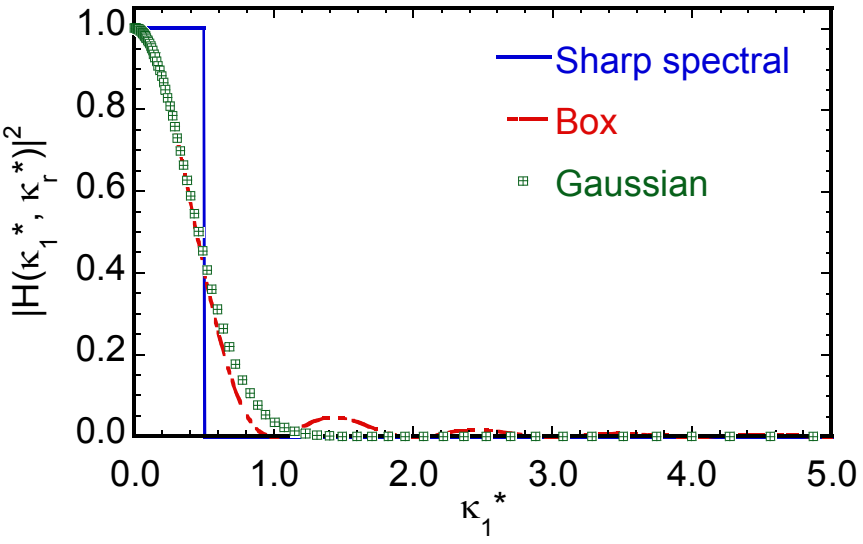

Figure 4 Magnitude-square of filter transfer functions to simulate the resolution effects with $\kappa_r^* = 0.5$.

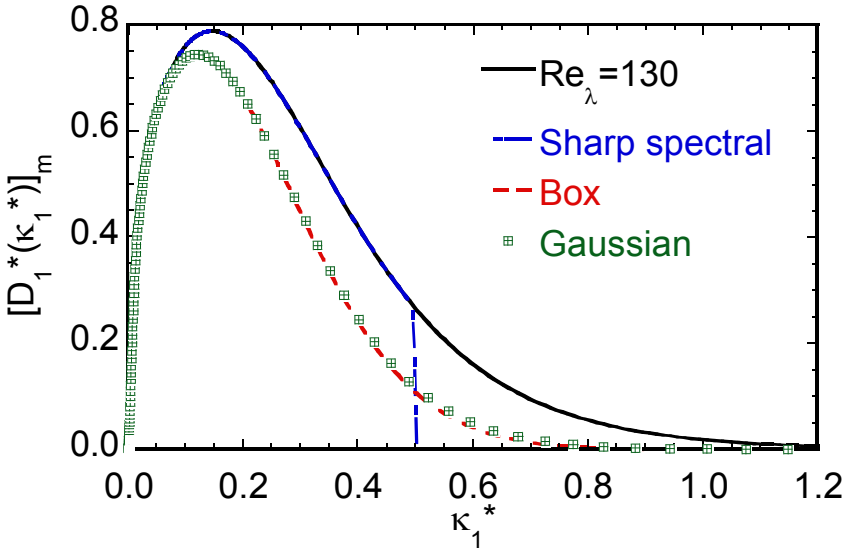

Figure 5 Spatial resolution effects on the 1D scalar dissipation spectrum at $\kappa_r^* = 0.5$. Model spectrum from Pope [38] is used with $\mathrm{Re}_\lambda = 130$.

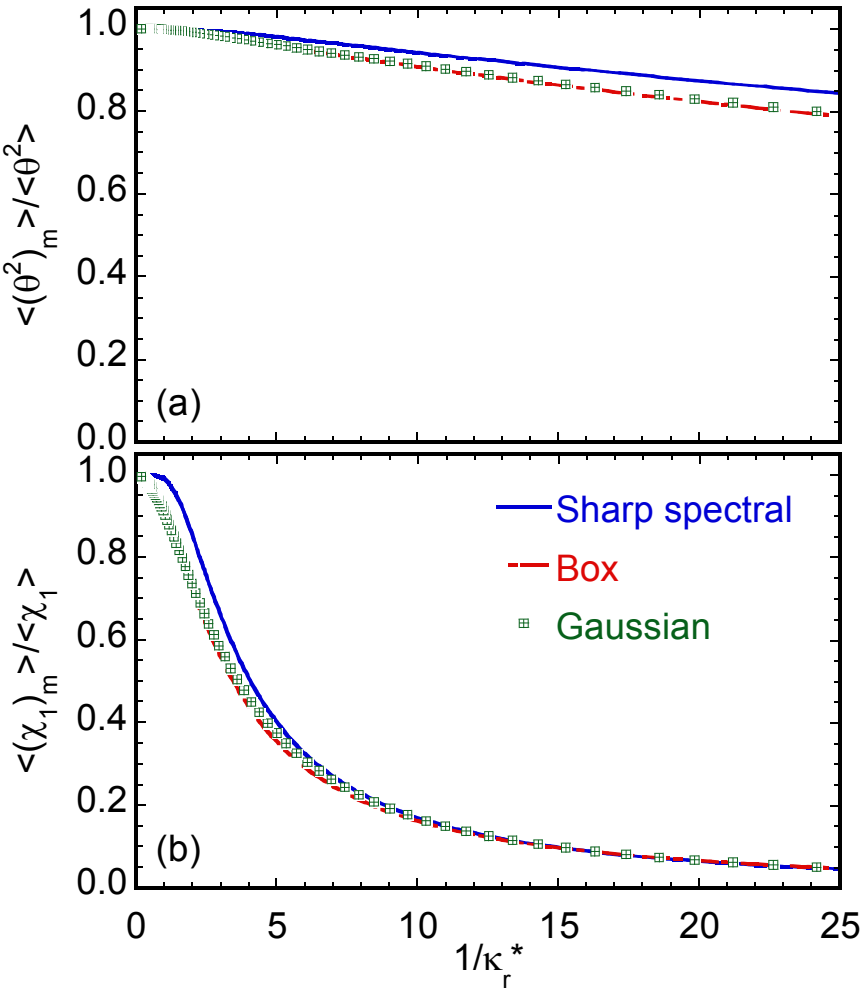

Figure 6 Effects of the spatial filter on the (a) scalar variance and (b) mean 1D scalar dissipation rate. Model spectrum from Pope [38] is used with $\mathrm{Re}_\lambda = 130$.

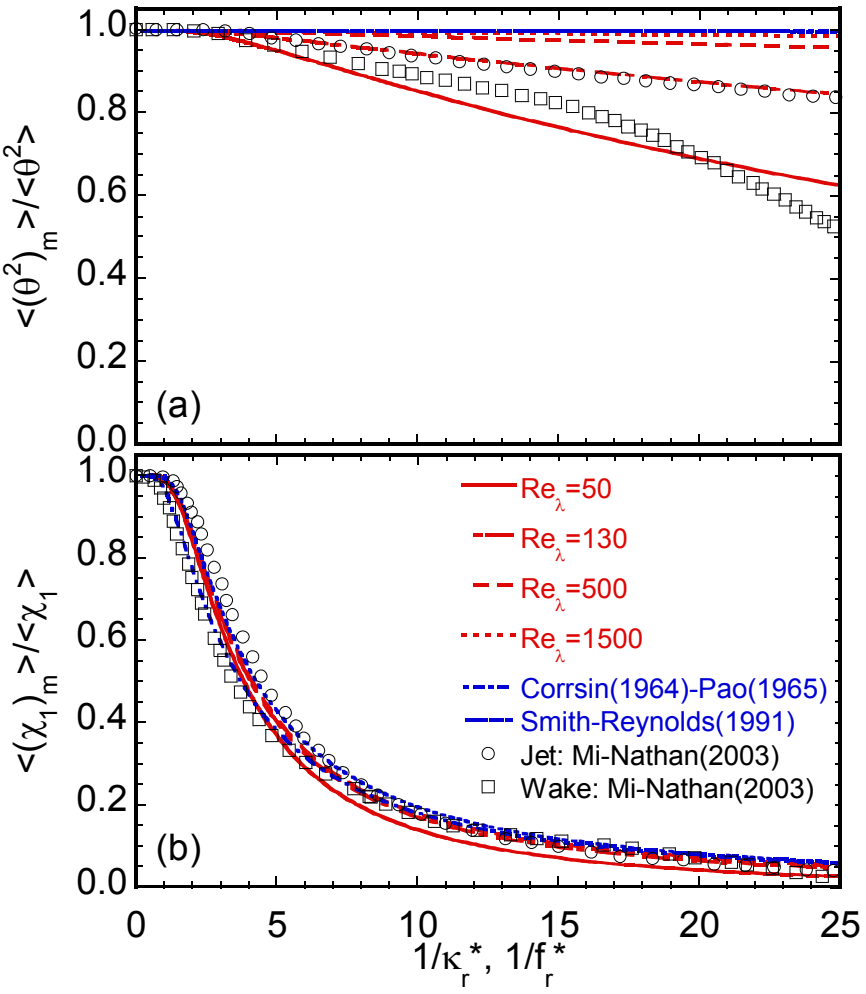

Figure 7 Effects of resolution on the measured (a) scalar variance and (b) mean 1D scalar dissipation rate. Model spectrum from Pope [38] is used with $Re_\lambda = 50$, 130, 500 and 1500.

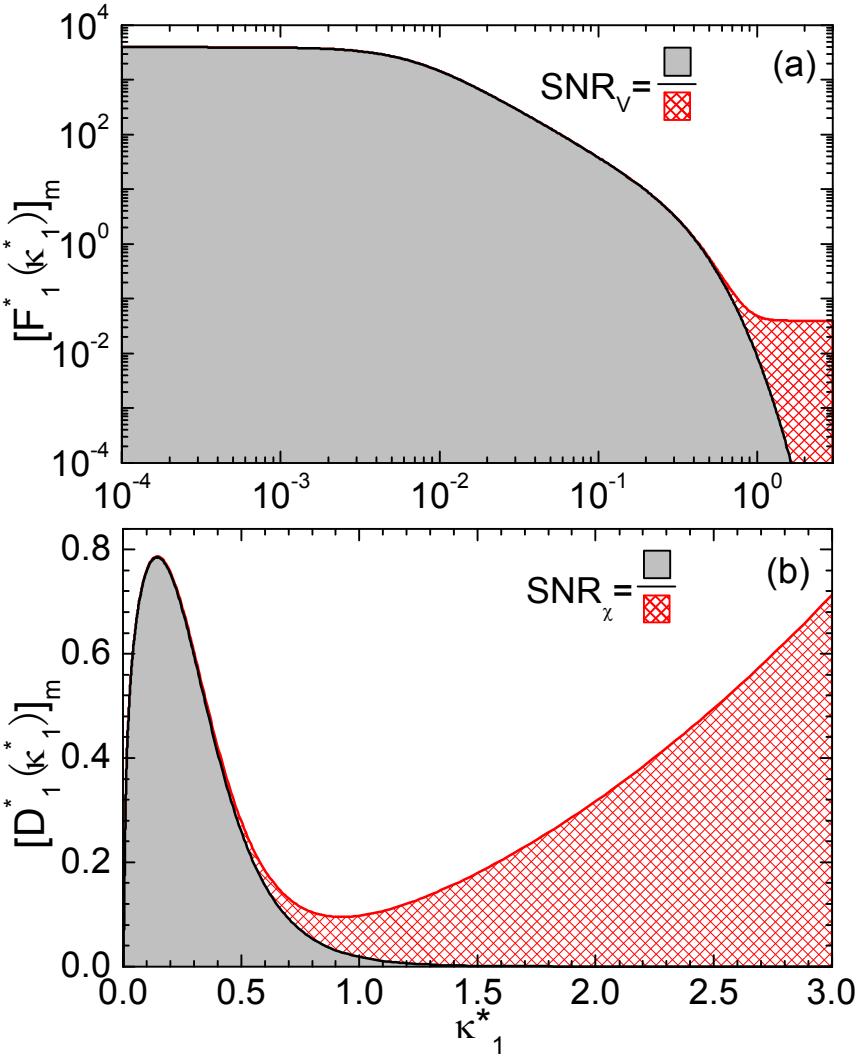

Figure 8 Illustration of noise effects on the measured 1D scalar energy and dissipation spectra. The integrations of the shade areas are the true scalar variance and mean dissipation rate; the integrations of "cross-filled" areas are the apparent variance and dissipation due to noise effect. SNRs for the turbulence variance (SNR_V) and dissipation rate (SNR_χ) are defined as the ratios of the integrated areas.

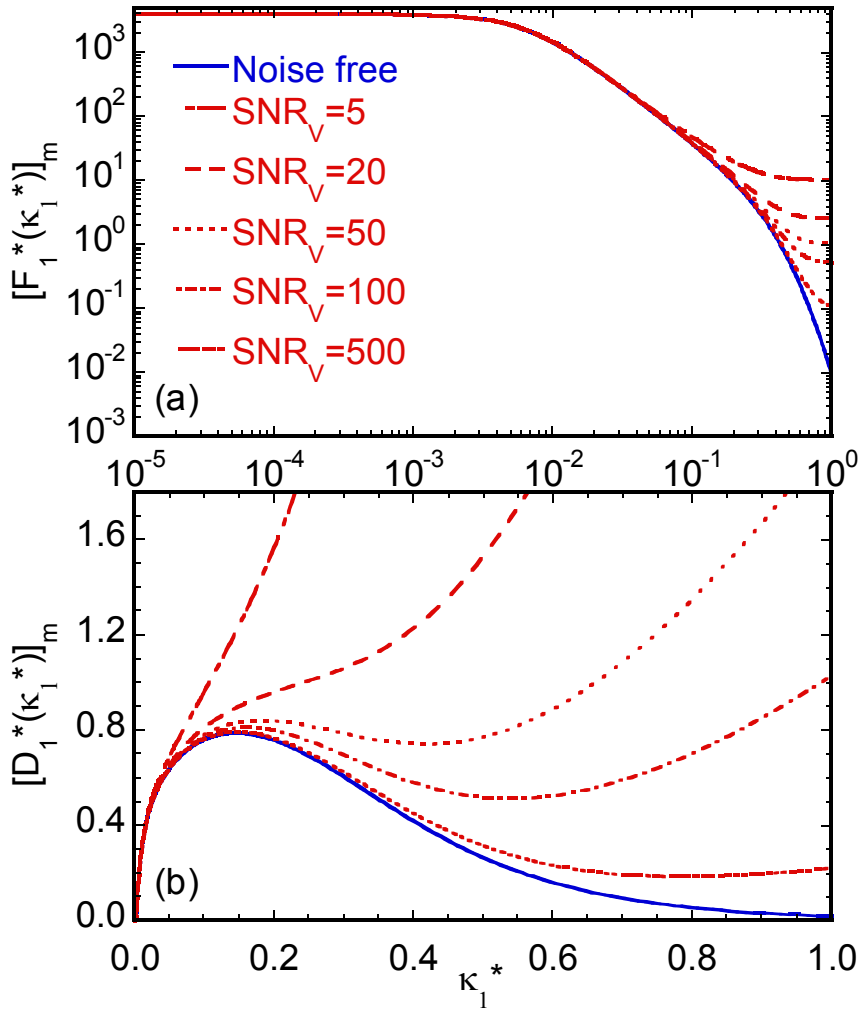

Figure 9 Effects of noise on the measured (a) 1D scalar energy spectra and (b) 1D scalar dissipation spectra at $\kappa_{1C}^* = 1$. Model spectrum from Pope [38] is used with $\mathrm{Re}_\lambda = 130$.

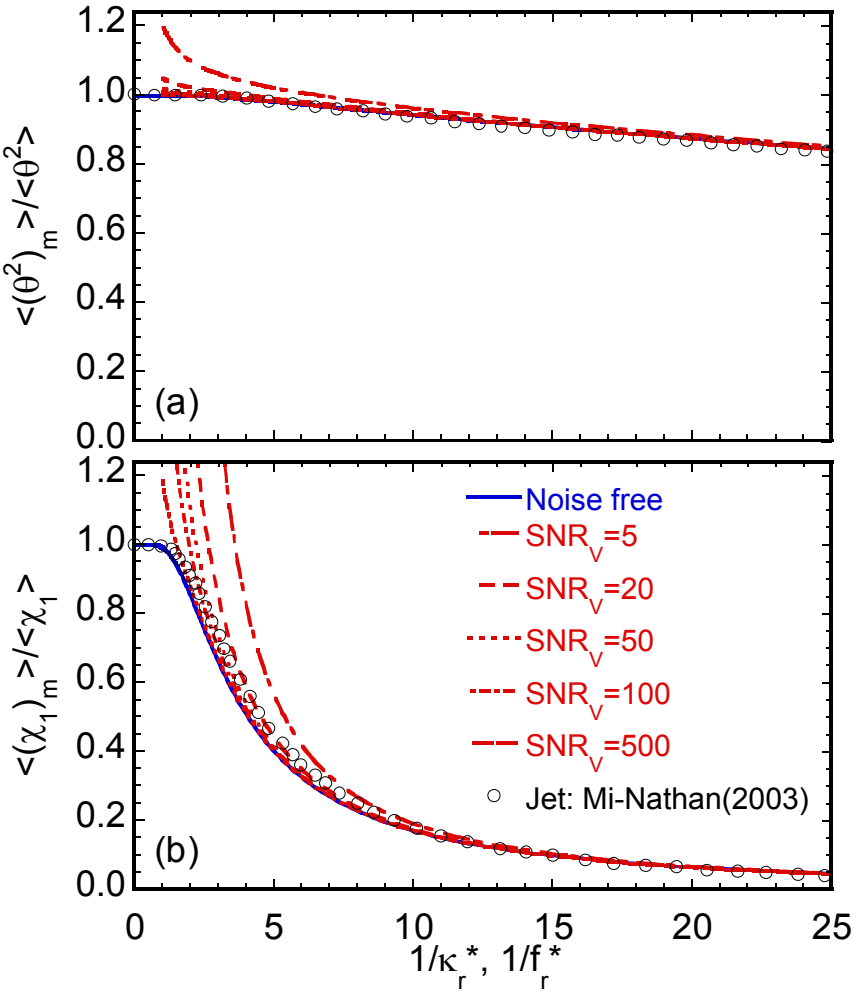

Figure 10 Effects of noise on the measured (a) scalar variance and (b) mean 1D scalar dissipation rate at $\kappa_{1C}^{*}=1$. Model spectrum from Pope [38] is used with $\mathrm{Re}_{\lambda}=130$.

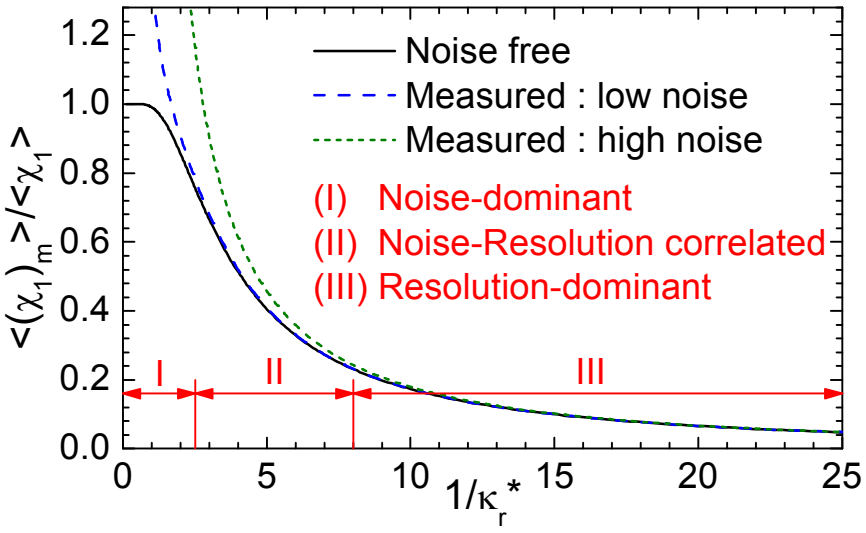

Figure 11 Illustration of the noise-resolution correlated effects on the 1D scalar dissipation measurement. The error curve can be divided into three regions: (I) noise-dominated; (II) noise-resolution correlated; (III) resolution dominated.

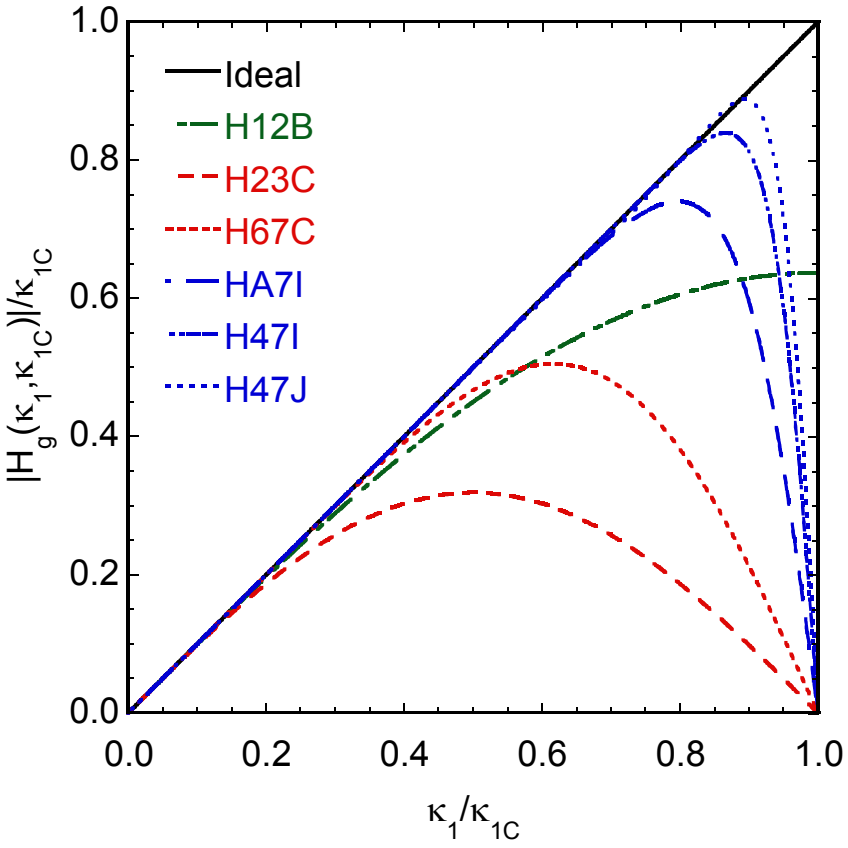

Figure 12 Magnitude response of the transfer functions for numerical stencils for gradient calculation.

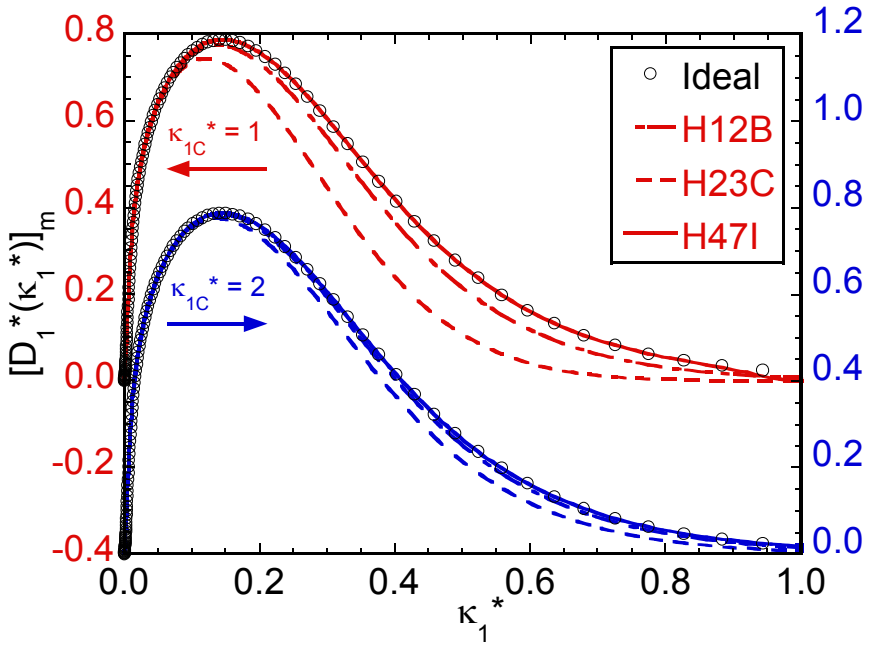

Figure 13 1D dissipation spectrum calculated with numerical stencils H12B, H23C, H47I with cutoff wavenumber $\kappa_{1C}^* = 1$ and $\kappa_{1C}^* = 2$, respectively. $\kappa_{1C}^* = 1$ is the ideal Nyquist sampling ($\kappa_{1S}^* = 2$), $\kappa_{1C}^* = 2$ is for over-sampling by a factor of two. H23C denotes the 2nd-order 3-point central-difference, H12B the 1st-order 2-point backward difference, H47I is the 4-th order 7-point implicit scheme. Model spectrum from Pope [38] is used with $\mathrm{Re}_\lambda = 130$.

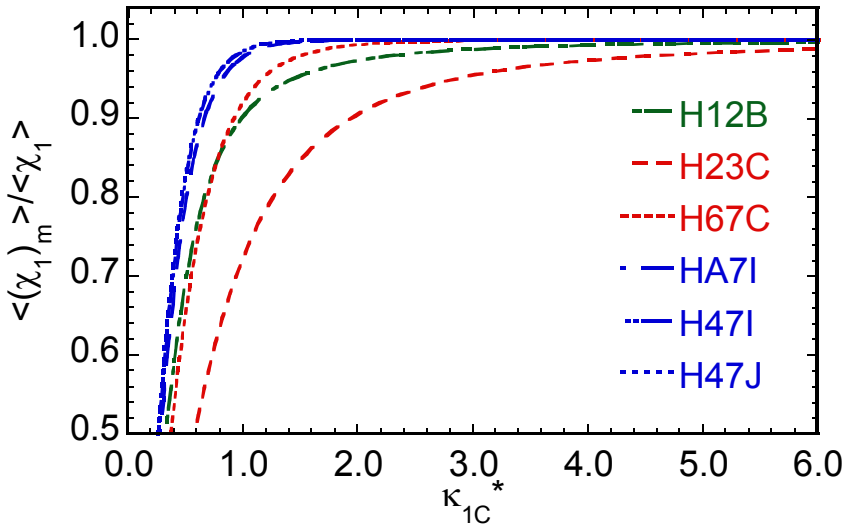

Figure 14 Effects of numerical stencils on the measured mean 1D scalar dissipation rate with varying cutoff wavenumber κ_{1C}^*. Here $\langle(\chi_1)_m\rangle$ is the mean dissipation rate at cutoff wavenumber κ_{1C}^*. Model spectrum from Pope [38] is used with $\mathrm{Re}_\lambda = 130$.

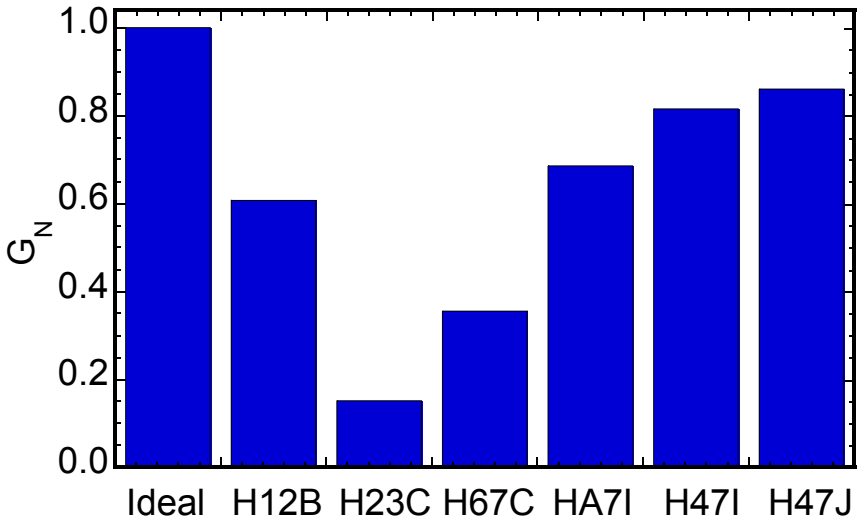

Figure 15 Noise amplification factors G_N for different numerical stencils.

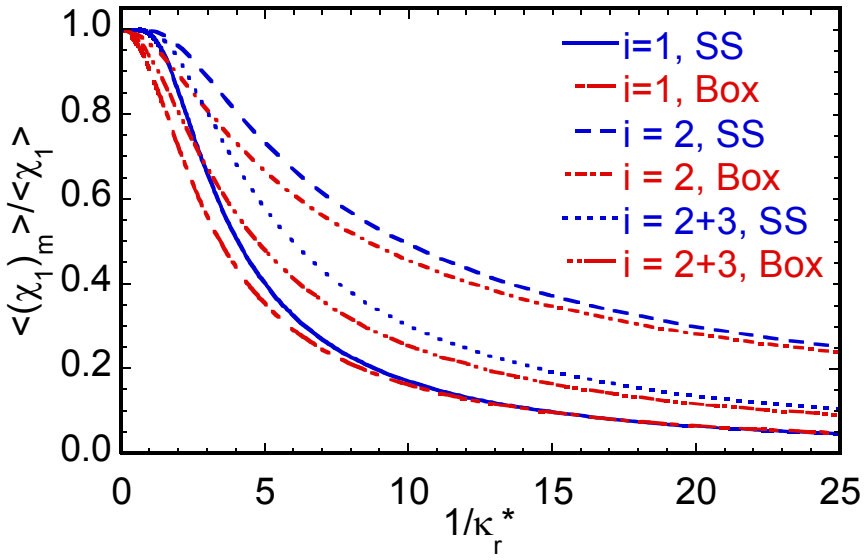

Figure 16 Comparison of the effects of resolution (e.g., averaging) on the 1D scalar dissipation rate in the direction of interest (x_1) and the two orthogonal directions (x_2 and x_3). $i = 1$ denotes the resolution effect in the measurement direction only, $i = 2$ is for averaging in the x_2 direction only, and $i = 2{+}3$ denotes averaging in the x_2 and x_3 directions only. The model spectrum from Pope [38] is used with $\mathrm{Re}_\lambda = 130$.

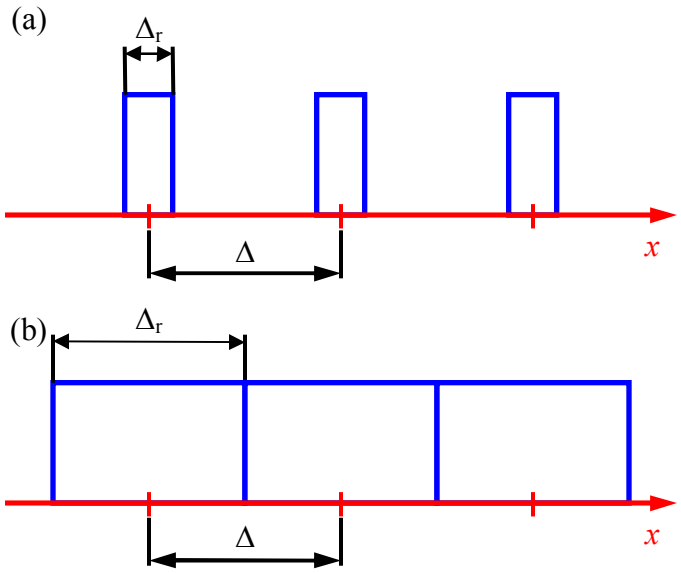

Figure 17 Illustration of the pixel binning effects: (a) 25% filling factor and (b) 100% filling factor. Δ_r is the effective sensor size (filter size), Δ is the pixel pitch (sampling resolution).

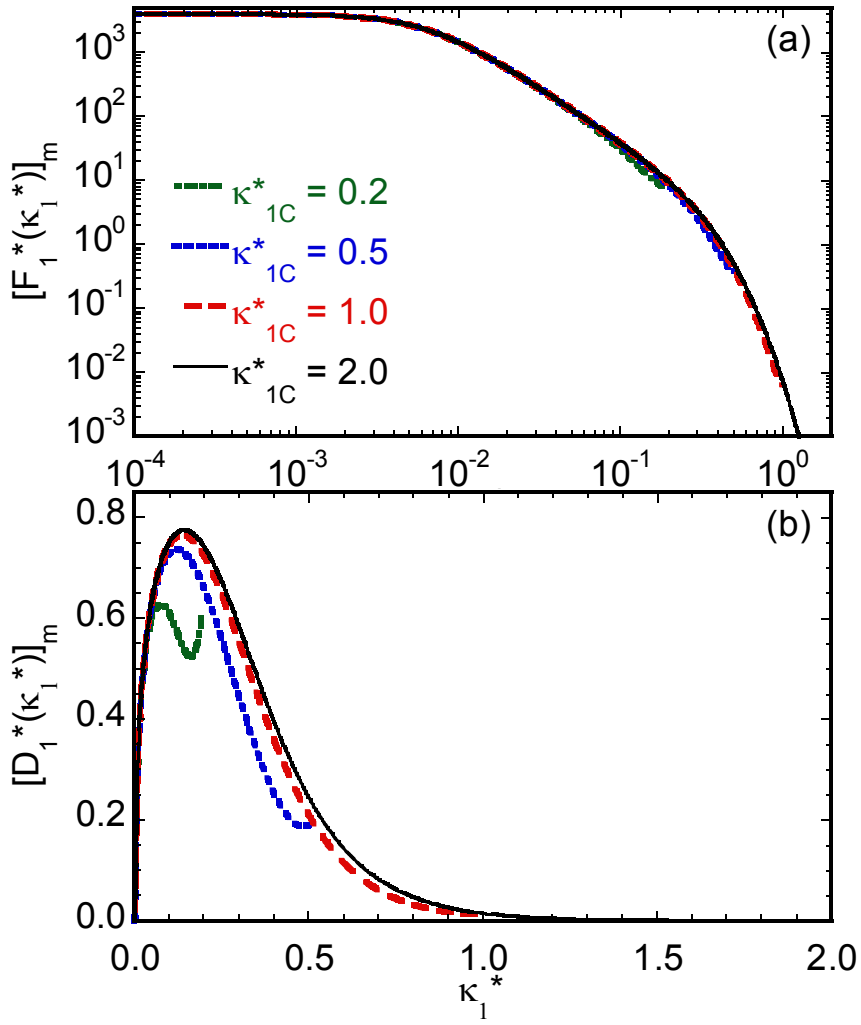

Figure 18 Effects of pixel-binning on the measured (a) scalar variance and (b) mean 1D scalar dissipation rate. Model spectrum from Pope [38] is used with $\mathrm{Re}_\lambda = 130$.

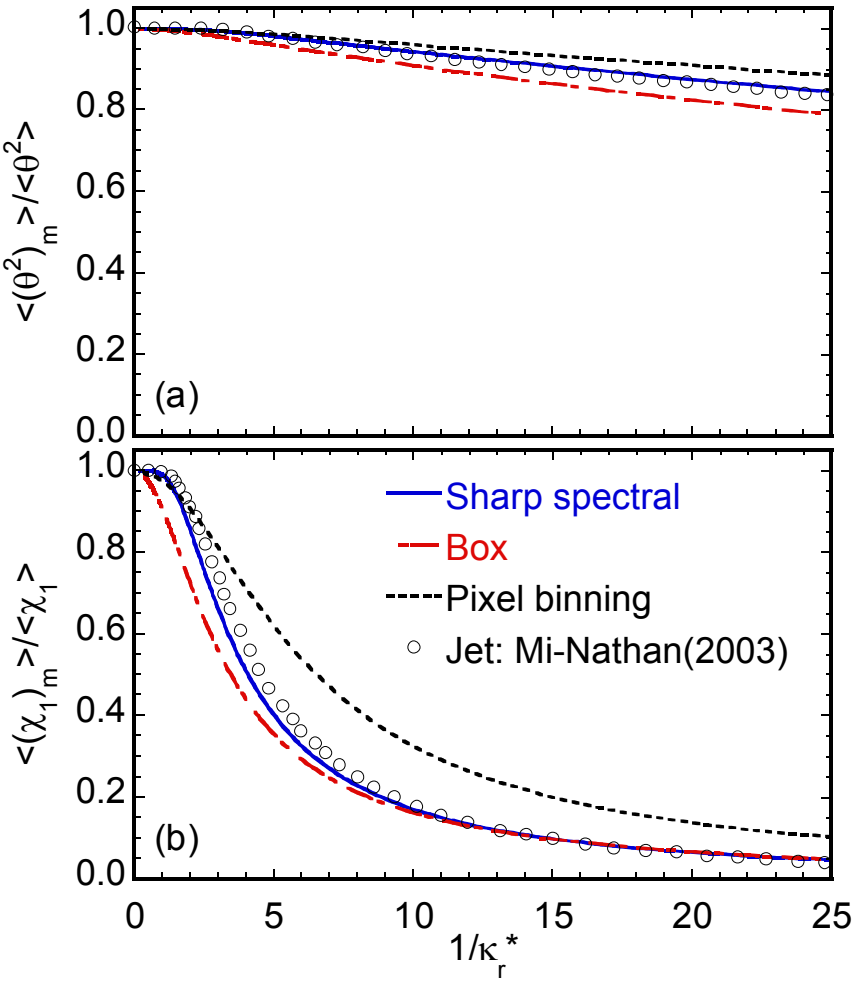

Figure 19 Effects of pixel-binning on the 1D measurements at $\mathrm{Re}_\lambda = 130$: (a) scalar variance and (b) 1D mean scalar dissipation rate.